DOI: 10.1002/ ((please add manuscript number))
Article type: Full paper

Boosting Superior Lithium Storage Performance of Alloy-based Anode Materials via Ultraconformal Sb Coating derived Favorable Solid-electrolyte Interphase

Bing-Qing Xiong, Xinwei Zhou, Gui-Liang Xu, Yuzi Liu, Likun Zhu, Youcheng Hu, Shou-Yu Shen, Yu-Hao Hong, Si-Cheng Wan, Xiao-Chen Liu, Xiang Liu, Shengli Chen, Ling Huang, Shi-Gang Sun, Khalil Amine,* and Fu-Sheng Ke**

B. Q. Xiong, Y. Hu, S. C. Wan, X. C. Liu, Dr. S. Chen, Dr. F. S. Ke
Sauvage Center for Molecular Sciences, College of Chemistry and Molecular Sciences, Wuhan University, Wuhan 430072, China
E-mail: kefs@whu.edu.cn
Dr. G. L. Xu, Dr. Xiang Liu, Dr. K. Amine
Chemical Sciences and Engineering Division, Argonne National Laboratory, 9700 S Cass Avenue, Lemont, Illinois 60439, USA
Email: xug@anl.gov, amine@anl.gov
X. Zhou, Dr. Y. Liu
Centre for Nanoscale Materials, Argonne National Laboratory, Lemont, IL 60439, USA
X. Zhou, Dr. L. Zhu
Department of Mechanical and Energy Engineering, Indiana University-Purdue University Indianapolis, Indianapolis, IN 46202, USA
Dr. S. Y. Shen, Y. H. Hong, Dr. L. Huang, Dr. S. G. Sun
State Key Laboratory of Physical Chemistry of Solid Surfaces, Department of Chemistry, College of Chemistry and Chemical Engineering, Xiamen University, Xiamen 361005, China
Dr. K. Amine
Materials Science and Engineering, Stanford University, Stanford, CA 94305, USA
IRMC, Imam Abdulrahman Bin Faisal University (IAU), Dammam, Saudi Arabia

Keywords: Antimony, Anode materials, Batteries, Solid electrolyte interphase, Catalytic decomposition

Alloy materials such as Si and Ge are attractive as high-capacity anodes for rechargeable batteries, but such anodes undergo severe capacity degradation during discharge-charge processes. Compared to the over-emphasized efforts on the electrode structure design to mitigate the volume changes, however, understanding and engineering of the solid-electrolyte interphase (SEI) have been

significantly lacking. This work manifests that modifying the surface of alloy-based anode materials by building an ultraconformal layer of Sb can significantly enhance their structural and interfacial stability during cycling. Combined experimental and theoretical study consistently reveal that the ultraconformal Sb layer is dynamically converted to Li_3Sb during cycling, which can selectively adsorb and catalytically decompose electrolyte additives to form a robust, thin and dense LiF-dominated SEI, and simultaneously restrain the decomposition of electrolyte solvents. Hence, the Sb-coated porous Ge electrode delivers much higher initial Coulombic efficiency of 85% and higher reversible capacity of 1046 mAh g^{-1} after 200 cycles at 500 mA g^{-1}, compared to only 72% and 170 mAh g^{-1} for bare porous Ge. The present finding has indicated that tailoring surface structures of electrode materials is an appealing approach to construct a robust SEI and achieve long-term cycling stability for alloy-based anode materials.

1. Introduction

Because of the explosive growing demand for portable electronic devices and pure/hybrid electric vehicles, there is a need for rechargeable batteries with higher energy density and greater safety.[1] Alloy materials MM' (M=Li, Na, K; M'= Sn, Si, Sb, Ge, P, etc.) offer higher theoretical capacities than that of the commercial graphite anode for rechargeable batteries.[2-5] The primary challenge to implement these alloy anodes in commercial batteries is their large volume change during the discharge-charge processes.[6-9] The repeated expansion/contraction results in the pulverization of the alloy materials, leading to the loss of electrical contact between the alloy particles and the current collector and further severe capacity degradation.[10, 11] To overcome this problem, past efforts have been focused on

controlling the size, composition, and morphology of those alloy anodes, including utilization of nano-sized materials and the design of unique nanoarchitecturing morphology.[10-21] For example, the capacity of Si nanowires after 10 cycles is ~3500 mAh g^{-1}, which is four times that of Si micrometer particles (~800 mAh g^{-1}).[13] However, those nanostructured alloy materials still suffer from rapid capacity degradation after prolonged cycling.[8, 10, 15, 22-26] In the past decades, compared to the over-emphasized efforts on the electrode structure design, the understanding and engineering of the electrode/electrolyte interface have been lacking.

The solid-electrolyte interphase (SEI) is a key component in rechargeable batteries. It results from the decomposition of electrolyte components (salt ions, solvents molecules, and functional additives), which forms a passivation layer on the surface of electrode materials. The constitution and structure of a SEI, generally including carbonaceous (e.g., $(CH_2OCO_2Li)_2$, $ROCO_2Li$, Li_2CO_3, and polycarbonates) and noncarbonaceous (e.g., LiF, Li_2O, LiOH) components, are dependent on the electrolyte. A compact, thin, and passivating SEI is necessary to enable the long-term operation of batteries beyond the thermodynamic limits of electrolytes, as is the case for the commercial graphite anode. The decomposition of solvent molecules is the most common pathway for the formation of the SEI.[27] However, for most alloy anode materials, continuous parasitic reactions between pulverized alloy particles and solvent molecules lead to thickening of the SEI and depletion of the electrolyte, eventually resulting in battery failure.[10] Hence, much effort has been focused on suppressing the decomposition of solvent molecules by tuning the electrolyte structure. One

strategy is to decompose the salt ions.[27-30] Recently, considerable effort has been focused on using high concentration electrolytes to restrain the decomposition of the solvent molecules. Such electrolytes can decrease the coordination number of lithium ions due to the scarcity of solvent molecules, which can result in a thinner LiF-rich SEI by shifting from a solvent decomposition to a salt anion decomposition/reaction.[27, 28, 30] However, there are still some disadvantages for the concentrated electrolyte, including precipitation of the Li salts at low temperature, difficulty for wetting cell separators and thick electrodes, and higher cost.[28] Another promising strategy is to decompose electrolyte additives.[31, 32] The use of electrolyte additives is the most economical and efficient method to modify the physical/chemical/mechanical properties of the SEI and thus improve the battery performance. For example, with fluoroethylene carbonate (FEC) additive, the composition of the SEI in the silicon anode is dominated by polycarbonate and LiF.[31] However, such an SEI is not flexible enough and cannot resist the dramatic volume changes of silicon, leading to a continuously growth of the SEI. Therefore, it is critical to construct a robust and compact SEI by guiding the decomposition of the electrolyte.

The electrochemical reduction of the electrolyte on the surface of electrode materials is an electrocatalytic process, which is significantly affected by both the electrolyte and the surface of the electrode material. For fuel cells, studies have shown surface dependence of kinetics and selectivity for the electrocatalytic oxidation of small organic molecules on noble metal catalysts.[33] Herein, we have adopted the concept of selectively catalytic electrolyte decomposition to control the SEI growth of alloy-based anode materials by tuning their

surface structures. We report a novel *in situ* strategy, for the first time, to build an interfacial layer between the alloy-based anode materials and the electrolyte. An ultraconformal layer of antimony was coated on both secondary/primary particles of a hierarchical porous Ge and Si electrodes. *In situ* powder X-ray diffraction (PXRD), on-line electrochemical mass spectroscopy (OEMS), X-ray photoelectron spectroscopy (XPS), and density functional theory (DFT) revealed that the Sb layer was lithiated to Li_3Sb during the initial discharge, which selectively adsorbed and decomposed the FEC to form a thinner LiF-rich SEI film, and restrainedly decomposed the solvents of ethylene carbonate (EC) and diethylene carbonate (DEC). Hence, both the initial Coulombic efficiency and cycling stability of the porous Ge and Si electrodes were remarkably improved due to the formation of a robust SEI through catalytic electrolyte decomposition.

2. Results and Discussion

2.1. Theoretical Understanding of the Function of Sb and Li_3Sb

The cracking and pulverizing of the alloy materials during cycling will result in forming nanosized materials. However, most of those *in situ* formed nanosized-alloy materials during discharge-charge process cannot stop the fast capacity decay except Sb. For example, the bulk Sb particles (~50 μm) sustained 600 mAh g^{-1} over 160 cycles, which are correspond to formation of crystal Na_3Sb.[35] Similarly, the electrochemical performance of bulk Sb particles (75 μm) are as well as nanosized Sb in both of LIBs and NIBs.[36] To understand this unique phenomenon of Sb, we employed DFT calculations to investigate the FEC and

EC adsorption on lower and higher Li concentrations in Sb electrode, and chose Ge as control electrode, i.e., the Li-covered Sb (111), Li-covered Ge (111), Li_3Sb (111), and Li_3Ge (111) surfaces. We calculated two orientations, i.e., parallel and vertical adsorption, of EC and FEC molecules on those surfaces with different binding energy (**Figure 1**a, Figure S1-S4 and Table S1, Supporting Information). The adsorption of EC and FEC molecules in parallel orientation is stronger than that of the vertical orientation on all of the above surfaces, which is similar to EC on the Si surface.[37] For the Ge surfaces, the EC molecule is always more easily adsorbed than the FEC molecule. At low Li concentration, adsorption of the EC molecule on the Sb (111) surface is favoured over the FEC molecule. However, at the full-lithiated condition (Li_3Sb), adsorption of the FEC over the EC molecule was favoured with a large binding energy (-1.060 eV), which is much larger than that of the EC molecule (-0.645 eV) on the Li_3Sb (111) surface. Meanwhile, the calculated data of crystal orbital Hamilton populations (COHP) also display the adsorption of FEC on Li_3Sb surface is always stronger than that of EC molecule (Figure S5 and Table S2, Supporting Information). This result illustrates that the FEC is much easier adsorbed on the Li_3Sb surface, which is converted from Sb during discharge. These adsorbed FEC molecules are therefore decomposed and formed LiF-rich SEI,[35, 36. 38] which can restrain the decomposition of EC molecules.[39-41] This effect may explain the previously reported good cycling stability of bulk micrometer-sized Sb electrodes for both lithium- and sodium-ion batteries.[35, 38] To enhance the electrochemical performance of other alloy electrodes, combining the unique Sb

with other alloy electrodes may be a feasible strategy. We chose porous Ge as an example to verify this strategy (Figure 1b).

2.2. Experimental Verfication

2.2.1. Structure Design and Characterization

Porous Ge and Sb-coated-porous Ge materials were synthesized by thermal reduction under hydrogen (see detail in the Experimental Section).[11] The structure and morphology of both anode materials were characterized by PXRD and scanning electron microscopy (SEM) (Figure S6, Supporting information). Compared to the PXRD pattern of porous Ge and Sb, the Sb-coated-porous Ge exhibits the typical peaks of Ge and Sb, indicating no formation of Sb-Ge alloy. Both bare porous Ge and Sb-coated-porous Ge have a hierarchical structure, which includes micro-sized secondary particles (10-20 μm) and nano-sized primary nanoparticles (Figure S6 and S7, Supporting Information). To directly observe the morphology and the distribution of the Sb layer throughout the outer and inner structure of the Sb-coated-porous Ge particle, a specimen was prepared and observed by scanning transmission electron microscopy combined with high-angle annular dark-field imaging (STEM-HAADF), as described in the Supporting Information. An ultraconformal layer of amorphous Sb with a thickness of ca. 4 nm was uniformly coated on both the inner and outer surface of the Ge particles (**Figure 2**a-c and Figure S8-10, Supporting Information), despite there was a small amount of Sb nanoparticles with size of < 10 nm in the Sb-coated-porous Ge particles (Figure S8, Supporting Information). The exact Sb content in the Sb-coated-

porous Ge compound was analyzed quantitatively by an electron probe micro-analyzer (Figure S11, Supporting Information), which shows 4.5 wt.% Sb in this compound. A high-resolution transmission electron microscopy (HR-TEM) image of the nanoparticle (Figure 2d) indicates that the distance between adjacent lattice planes is ~0.327 nm, in good agreement with the d-spacing of the (111) plane of Ge.

2.2.2 Electrochemical characterization

The electrochemical properties of the Sb-coated-porous Ge electrode was evaluated in coin cell tests, which were performed within a potential window of 0.01 to 2.0 V vs. Li/ Li^+ under different current densities (**Figure 3** and Figure S12, Supporting Information). Use of bare porous Ge was chosen for a control experiment under identical conditions. Figure 3a shows the initial voltage profile of the Sb-coated-porous Ge and uncoated Ge electrodes at 500 mA g^{-1}. Compared to the voltage curve of bare porous Ge, that of the coated electrode shows extra small plateaus at ~0.75 and 1.0 V vs. Li/ Li^+ during the first discharge and charge, as indicated in the differential capacity plots (Figure S12c and d, Supporting Information), corresponding to the lithiation/delithiation of Li_3Sb/Sb. The first discharge capacities of the Sb-coated-porous Ge and bare porous Ge electrodes are 1623 and 1680 mAh g^{-1}, and their first charge capacities are 1376 and 1210 mAh g^{-1}, which result in initial Coulombic efficiencies of 85.0 and 72.0%, respectively. The irreversible capacity may be caused by the decomposition of the electrolyte to form SEI passivation films. The results indicate that more solvents were decomposed in the bare porous Ge compared to the Sb-coated-porous Ge electrode. After 200 cycles, the reversible capacity of the Sb-coated-porous Ge electrode

is as high as 1046 mAh g^{-1}, but only 170 mAh g^{-1} for bare porous Ge despite it having a hierarchical micro/nanostructure (Figure 3b), which has been frequently reported to be able to mitigate the volume changes. These results demonstrate that the ultraconformal Sb layer at both primary/secondary particles level can significantly improve the cycling stability of the porous Ge electrode.

To further explore the effect of the ultraconformal Sb layer at different current densities, we evaluated the cycling performance of the electrode materials at 100 and 1000 mA g^{-1}, as shown in Figure 3c and d. The charge capacity of the Sb-coated-porous Ge electrode is 1200 and 1010 mAh g^{-1} after 200 cycles at 100 and 1000 mA g^{-1}, which are 94% and 91% of the first charge capacity, respectively. By contrast, the corresponding capacity retentions for bare porous Ge electrodes are only 12% and 9% under identical conditions. More interestingly, compared to both differential capacity plots (Figure S12c and d, Supporting Information), the peak located at 0.64 V, corresponding to the extraction of Li from crystal $Li_{15}Ge_4$ to Ge,[34, 42-45] disappeared after the first cycle in the Sb-coated-porous Ge electrode. However, in the bare Ge electrode, this peak remained even after 50 cycles. It is inferred that crystal $Li_{15}Ge_4$ and amorphous $Li_{15}Ge_4$ (or Li-Ge alloy) formed in the bare and Sb-coated-porous Ge electrodes after the second cycle, respectively. This phenomenon was also observed in the Si electrode.[26] The differential capacity plots indicate that the ultraconformal Sb layer has changed the Li storage mechanism of Ge, which will be discussed later in more detail. More interesting, this strategy, building an ultraconformal Sb

layer, is also suitable for high capacity Si-based anode according to our preliminary data (Figure S13, Supporting Information).

2.2.3 Structure characterization during discharge-charge

We carried out *in situ* PXRD and *in situ* SEM studies of the Sb-coated-porous Ge electrode to investigate the structural changes in both the bulk electrode and a single particle during cycling. **Figure 4**a shows the contour map of *in situ* PXRD and the corresponding discharge-charge curves of the electrode at the first two cycles. The unchanged peaks at 22.8°, 28.7°, 41.3°, 43.1°, 45.8°, 50.1°, 51.1°, and 52.9° can be assigned to BeO, Be, or the substrate of the *in situ* XRD cell. The change of colour in peaks reflects a phase transition. During the first discharge, a new peak (light red) appeared at 23.4°, equivalent to discharge to 0.74 V vs. Li/Li^+. Meanwhile, the diffraction peaks of Sb disappeared. This peak can be assigned to the (111) reflection of Li_3Sb (PDF # 03-065-3011). When discharged to 0.35 V, the intensity peak at 23.4° continuously increased, while another new broad peak at 20.0-23.0° appeared, suggesting formation of Li_xGe phases. At the end of the initial discharge, a much clearer peak appeared at ~23.4°, ascribed to the (111) peak of Li_3Sb and $Li_{15}Ge_4$ (PDF # 01-089-2584) (Figure S14, Supporting Information). A broad peak at 20.0-23.0°, corresponding to amorphous/nanocrystal $Li_{15}Ge_4$, is consistent with the differential capacity plots (Figure S12c, Supporting Information). The intensity of the Ge peaks had clearly decreased, but they still existed during the first discharge because of the high mass loading (~6 mg cm^{-2}) of the working electrode needed to obtain a stronger diffraction signal. During

the charge, the broad peak at 20.0-23.0° disappeared, and the intensity of the diffraction peak of 23.4° decreased when the electrode was charged to 0.75 V, which suggests the oxidation of Li_xGe to Ge. At the end of the first charge, the (111) peak of Li_3Sb completely disappeared, while the peak of Sb emerged again. This finding indicates that the delithiation of Li_3Sb can be converted back to crystal Sb. We concluded that the phase transition between crystal Sb and crystal Li_3Sb is reversible in lithiation/delithiation cycles (Figure S14, Supporting Information), suggesting that the ultraconformal Sb layer had converted to a Li_3Sb. The Sb layer was uniform coated on the Ge particles after one cycle (Figure S15, Supporting Information). During the subsequent cycle, similar phenomena were consistently observed.

To study the function of the ultraconformal Sb layer, we used *in situ* PXRD of the bare porous Ge electrode as the control experiment under identical conditions (Figure S16, Supporting Information). The crystal $Li_{15}Ge_4$ (PDF # 01-089-2584) was evident in the second cycle, which is consistent with previous results.[44, 45] This result is in good agreement with the differential capacity plots (Figure S12c and d, Supporting Information). The *in situ* PXRD and differential capacity plots confirmed that the Sb skin layer changes the Li storage mechanism of Ge in the Sb-coated-porous Ge electrode. Furthermore, we analysed the intensity of the Ge (111), (220), and (311) reflection peaks in the first 120 scans during the initial discharge of the Sb-coated-porous Ge electrode (Figure S17, Supporting Information). The intensity of the three peaks decreased at the same rate. This finding indicates that the Li ions react with Ge at the same speed from different directions,

i.e., isotropic lithiation in the Sb-coated-porous Ge material, which is similar to the results from the bare porous Ge electrode (Figure S18, Supporting Information) and consistent with previous results.[42, 43]

In order to directly observe the morphological change of the Sb-coated-porous Ge during the discharge/charge process, we have conducted a single particle morphology measurement during discharge-charge through *in situ* SEM. Figure 4b-h display the initial discharge-charge curve of a single Sb-coated-porous Ge particle at low current (400 pA) and the corresponding *in situ* SEM images at different discharge/charge stages. The SEM results showed that the volume increases during discharge. At the end of the first discharge, the volume increased to 290%, which is much less than the bare porous Ge particle (360%, Figure S19, Supporting Information) and the previous result (370%).[46, 47] When lithium is removed from the particle, the volume decreases, but it is a little larger than that of the initial stage at the end of charge. Note that no pulverization or cracks were observed on the particle during the whole discharge/charge process. To check the inner structure changes of this particle after the initial charge, we used a focused ion beam to cut the particle and SEM to observe the morphology (Figure 4i). Compared to the initial state (Figure S7, Supporting Information), the porous structures were still well maintained after one cycle of discharge-charge. This result indicates that the porous structure and suppressed side reactions can buffer the large volume change, which supported by the SEM images after 20 cycles (Figure S20, Supporting Information). Furthermore, we analysed the particle size evolution at different lithiation/delithiation stages from two directions (Figure 4c). Figure 4j shows that

size change in both directions is almost synchronous, suggesting that the insertion and extraction of lithium ions in the particles are at the same speed in all directions. This phenomenon was also observed in another Sb-coated-porous Ge particle and the bare porous Ge particle (Figure S19 and S21, Supporting Information). The results demonstrate that the lithiation/delithiation in the Sb-coated-porous Ge material is isotropic, which is consistent with the *in situ* XRD analysis (Figure S17, Supporting Information).

2.2.4 Characterization of Interface

OEMS was further used to track the gaseous products during the initial discharge, which were formed as a result of the decomposition of the solvent molecules. **Figure 5**a and b compare the OEMS results for the Sb-coated and bare porous Ge electrodes. The blue and green curves of m/z are 44 and 28, which can be ascribed to CO_2 and CO gas (Figure S22, Supporting Information), respectively. In the Sb-coated-porous Ge electrode, CO_2 gas is observed at the discharge potential of 0.75 V, which corresponds to the lithiation of Sb (Figure S12, Supporting Information) and suggests that the solvent molecules decomposed at this potential. However, this CO_2 peak appeared at a lower discharge potential of 0.6 V in the bare porous Ge electrode. More importantly, the intensity and area of this peak are much higher than those of the Sb-coated-porous Ge (Table S3, Supporting Information), indicating much more solvent molecule decomposition in the former electrode. We concluded that the Sb/Li_3Sb skin layer could significantly suppress the solvent molecule decomposition.

To elucidate the precise chemical composition of the SEI layer, we used XPS to check the chemical bonding environments of the species involved. Figure 5c-h display the deconvolution of the C 1s, Ge 2p, and F 1s XPS spectra of the samples discharged to 0.01 V. Except for the reference peak at 284.8 eV, the deconvolution of the C 1s spectrum shows a chemical environment consistent with that of the decomposed solvent molecules (Figure 5c and f), dominated by the formation of RO-CO_2Li and C-O-C.[48] Compared to the reference peak, the intensity of those two peaks is much lower in the Sb-coated-porous Ge than that of the bare porous Ge electrode. This result confirmed much less solvent decomposition in the former electrode, which is consistent with the OEMS data (Figure 5a and b). Furthermore, the deconvolution of the Ge 2p spectra displays metal Ge and Li-Ge peaks for the Sb-coated-porous Ge electrode (Figure 5g), but no Ge peak for the bare porous Ge electrode (Figure 5d). Combined to the OEMS result, maybe the SEI thickness in the bare porous Ge electrode is larger than in the Sb-coated-porous Ge electrode.

To understand the function of the Sb/Li_3Sb skin layer, we analyzed the F 1s XPS spectra after initial full discharge of both samples. The deconvolution of the F 1s spectra shows that the SEI layer contains LiF and C-F in the bare Ge electrode (Figure 5e), but only LiF in the Sb-coated-porous Ge electrode (Figure 5h). This result illustrates that the FEC in the electrolyte was completely converted to LiF, i.e., LiF-rich SEI, in the Sb-coated-porous Ge electrode. We further analysed the F 1s XPS spectra after 10 cycles, which still displayed only LiF even after sputtering time of 100s (Figure S23, Supporting Information). The intrinsic electrochemical stability of the Li-rich SEI film can prevent further side reactions

between electrolyte and electrode.[49] When discharged to 0.5 V, i.e., the Sb skin layer had completely lithiated to Li_3Sb, the C-F peak was still observed (Figure S24, Supporting Information), suggesting that the Li_3Sb completely catalysed C-F to Li-F during the subsequent discharge. This phenomenon was observed in the pure Sb electrode (Figure S25a and b, Supporting Information), which was supported by the initial discharge-charge profiles of pure Sb electrode with / without FEC electrolyte (Figure S26, Supporting Information), while it did not happen in the bare porous Ge electrode (Figure S25c and d, Supporting information). The XPS results suggest that the Li_3Sb can completely catalytically decompose the C-F to Li-F and, hence, form a LiF-rich SEI layer. Meanwhile, the LiF-rich SEI layer restrains the decomposition of solvent molecules,[39-41] such as EC and DEC, leading to a thinner and denser SEI layer. This result was supported by the poor cycling performance of the Sb-coated-porous Ge electrode without FEC electrolyte (Figure S26, Supporting Information). This effect is believed to be the key factor in achieving the excellent performance in the Sb-coated-porous Ge electrode. Without the surface modification of Sb, the bare hierarchical porous Ge electrode forms a much thicker and organic-phase dominated SEI, leading to continuous capacity degradation during cycling.

3. Conclusion

In summary, we reported a surface-controlled SEI growth in alloy anode materials. By tailoring the surface of a Ge electrode with an ultraconformal Sb layer, this electrode can selectively decompose electrolyte additives rather than solvent molecules, leading to the formation of a robust, thin, and dense LiF-dominated SEI and remarkably improved initial

Coulombic efficiency and cycling stability. This work has shed new light on how surface engineering can be used to tailor the composition and mechanical properties of the SEI, which may enable the use of micro-sized alloy anodes to significantly increase their volumetric energy density. The present findings will also stimulate more research regarding the low initial Coulombic efficiency and the fading mechanism of nanostructured alloy anodes, such as silicon, which is a very promising anode material for the next-generation lithium-ion batteries with specific energy of 500 Wh kg^{-1}.

4. Experimental Section

Synthesis of porous Ge: Porous Ge was synthesized according to a method in the literature.[11] Typically, porous Ge particles were fabricated by the thermal reduction of GeO_2 (99.99%, Alfa Aesar) in a tube furnace with flowing H_2 at 450°C for 12 hours, and then cooled to room temperature. The pressure of hydrogen was approximately 1 bar.

Synthesis of Sb-coated-porous Ge: $C_8H_4K_2O_{12}Sb_2$ (99.5%, Aladdin) solution (350 μL, 80 mg mL^{-1}) was dropped in 100 mg of porous Ge. The composite was dried in a vacuum oven, and then thermally reduced in a tube furnace with flowing H_2 at 450°C for 6 hours to obtain the Sb-coated-porous Ge.

Characterization: PXRD experiments were carried out on a Rigaku Smartlab with filtered Cu Kα radiation (λ = 1.5405 Å). The morphology of the samples was characterized by field emission SEM (Zeiss Ltd.) operated at 20 kV. A Zeiss NVision 40 FIB/SEM dual beam system was employed to prepare a TEM specimen of Sb-coated-porous Ge particle through a standard lift-out procedure. To reveal the spatial distribution of the Sb skin layer, a FEI Talos F200X (S) TEM equipped with

SuperX energy-dispersive X-ray spectrometer was used for high angle annular dark-field (HAADF) imaging and elemental mapping. An electron probe micro-analyzer (JXA-8530F Plus) was applied to analyze the concentration of Sb in the Sb-coated-porous Ge sample. XPS analyses were carried out on an ECSALAB 250Xi high performance electron spectrometer (Thermo Fisher Company).

Electrochemistry: Electrochemical experiments were carried out in CR2016-type coin cells. The Sb-coated or uncoated porous Ge were mixed with BP2000 carbon black and poly (acrylic acid) (average Mw ~450,000, Sigma-Aldrich) binder in N-methyl-1,2-pyrrolidinone (99%, Sigma-Aldrich) with mass ratio of 80:10:10 to form a slurry. The slurry was coated onto Cu foil current collectors and dried at 80 °C for 12 h under vacuum. The mass loading of the composite electrodes ranged from 1.0 to 1.5 mg cm^{-2}. The CR2016-type coin cells were assembled in an argon-filled glove-box using Li foil as the counter electrode and Celgard 2400 as the separator. The electrolyte consists of a solution of $LiPF_6$ (1.0 M) in a mixture of ethylene carbonate (EC)/diethyl carbonate (DEC) 1:1 (vol %) containing 5 wt% fluoroethylene carbonate (FEC). The cells were galvanostatically discharged-charged on a battery test system (SLAN BT100, Wuhan) between 0.01 and 2.0 V at room temperature.

The setup of the *in situ* SEM for a single Sb-coated Ge particle during charge/discharge can be found in our previous work.[50] Typically, to build a single-particle battery cell, a Sb-coated porous Ge particle is attached to a tungsten probe by ion beam carbon deposition as the positive electrode. Lithium metal is placed on top of the SEM stub as the negative electrode. One drop of ionic liquid electrolyte (ILE) is placed on top of the Li metal. The single-particle battery cycling is controlled by a Keithley 6430 sub-femtoamp remote SourceMeter from Tektronix. The

particle is immersed in the ILE drop during cycling and lifted out for imaging at different states of charge and discharge. To visualize the microstructure change of the particle, the imaging area is polished by a focused ion beam to remove the ILE from the surface.

The *in situ* PXRD experiment was manipulated with a home-made appliance, and a Sb-coated-porous Ge slurry was coated onto copper nets in an argon-filled glove-box, where beryllium (Be) was used as an X-ray transmissive window. The *in situ* XRD was carried out on a Smart-lab instrument (Rigaku) with filtered Cu Kα radiation (λ = 1.5405 Å, Rigaku D/max-2500) and a power of 9 kW (45 kV, 200 mA). *In situ* XRD was performed with repeated sequential scans, with each scan collected between 18° and 55° at a scanning speed of 20° min^{-1} and step size of 2θ = 0.01°.

The OEMS experiment was conducted in a custom-made cell, which was assembled in an argon-filled glove-box. Pre-dehydrated helium (99.999%) was employed as the carrier gas. A high flow rate was used to purge the pipeline to remove the air. Then, the flow rate was controlled at 8 mL min^{-1} by a gas controller. The gas products during the discharge were carried to pass through a cold trap (mixture of dry ice and ethanol) to condense the electrolyte vapor before entering the mass spectrometer (modified 5975C mass-selective detector, Agilent)[51].

Calculation Methods: The Pwscf code of the QUANTUM-ESPRESSO package under the generalized gradient approximation, the Perdew-Burke-Ernzerhof functional,[52, 53] and the ultrasoft pseudopotentials were used for all the DFT calculations which considered spin-polarization, in which the kinetic energy cutoff and charge-density cutoff were 30 Ry and 300 Ry, respectively. The smearing parameter was 0.01 Ry while the threshold of the self-consistent field and relax were 10^{-6} Ry and default in PWscf. Two simple models were built to describe the change in the structure of

the electrode material after Li insertion by decrease of potential: a three-layer slab model of Sb/Ge(111)-(2×2) with single adatom Li and a three-layer slab model of Li_3Sb/Li_3Ge(111)-(2×2). In the slab model, the top two layers were allowed to relax while the bottom one was fixed, and a vacuum region of 15 Å was set in the Z-direction to eliminate the influence between the bottom and top layers. For structural optimizations of all the models, 4×4×1 Monkhorst-Pack k-point meshes were used.

Supporting Information

Supporting Information is available from the Wiley Online Library or from the author.

Acknowledgements

B.Q.X and X.Z contributed equally to this work. We thank Dr. Chao Wang, Dr. Hengjiang Cong and Dr. Hexiang Deng (Wuhan University) for their invaluable assistance. This work was sponsored by National Nature Science Foundation of China (21403157, 21773176), and the Fundamental Research Funds for the Central Universities (2042017kf0232, 2042019kf0200). F.S.K. acknowledges the New Faculty Startup Fund of Wuhan University, Large-scale Instrument and Equipment Sharing Foundation of Wuhan University. DFT calculations in this paper have been done on the supercomputing system in the Supercomputing Center of Wuhan University. This work was also partially supported by National Science Foundation under Grant Number CBET1408751. Research at the Argonne National Laboratory was funded by the U.S. Department of Energy (DOE), Vehicle Technologies Office. Use of the Centre for Nanoscale Materials, Office of Science user facilities, was supported by the U. S. Department of Energy, Office of Science, and Office of Basic Energy Sciences, under Contract No. DE-AC02-06CH11357. K.A. and G.L.X. also thank the support from Clean Vehicles, US-China Clean Energy Research Centre (CERC-CVC2).

Conflict of Interest

The authors declare no conflict of interest.

Received: ((will be filled in by the editorial staff))
Revised: ((will be filled in by the editorial staff))
Published online: ((will be filled in by the editorial staff))

References

[1] X. Liu, D. Ren, H. Hsu, X. Feng, G. L. Xu, M. Zhuang, H. Gao, L. Lu, X. Han, Z. Chu, J. Li, X. He, K. Amine, M. Ouyang, *Joule* **2018**, *2*, 2047.

[2] J. Wang, C. Eng, Y. K. Chen-Wiegart, J. Wang, *Nat. Commun.* **2015**, *6*, 7496.

[3] W. Zhang, J. Mao, S. Li, Z. Chen, Z. Guo, *J. Am. Chem. Soc.* **2017**, *139*, 3316.

[4] Q. Zhang, H. Chen, L. Luo, B. Zhao, H. Luo, X. Han, J. Wang, C. Wang, Y. Yang, T. Zhu, M. Liu, *Energy Environ. Sci.* **2018**, *11*, 669.

[5] Y. Wu, Q. Pan, F. Zheng, X. Qu, C. Yang, X. Xiong, M. Liu, D. Hu, C. Huang, *J. Alloys Compd.* **2018**, *744*, 481.

[6] S. W. Lee, M. T. McDowell, L. A. Berla, W. D. Nix, Y. Cui, *Proc. Natl. Acad. Sci.* **2012**, *109*, 4080.

[7] X. H. Liu, J. W. Wang, S. Huang, F. Fan, X. Huang, Y. Liu, S. Krylyuk, J. Yoo, S. A. Dayeh, A. V. Davydov, S. X. Mao, S. T. Picraux, S. Zhang, J. Li, T. Zhu, J. Y. Huang, *Nat. Nanotech.* **2012**, *7*, 749.

[8] S. W. Lee, H. W. Lee, I. Ryu, W. D. Nix, H. Gao, Y. Cui, *Nat. Commun.* **2015**, *6*, 7533.

[9] Y. Yuan, K. Amine, J. Lu, R. Shahbazian-Yassar, *Nat. Commun.* **2017**, *8*, 15806.

[10] F. S. Ke, L. Huang, L. Jamison, L. J. Xue, G. Z. Wei, J. T. Li, X. D. Zhou, S. G. Sun, *Nano Energy* **2013**, *2*, 595.

[11] F. S. Ke, K. Mishra, L. Jamison, X. X. Peng, S. G. Ma, L. Huang, S. G. Sun, X. D. Zhou, *Chem. Commun.* **2014**, *50*, 3713.

[12] A. S. Aricò, P. Bruce, B. Scrosati, J. M. Tarascon, W. van Schalkwijk, *Nat. Mater.* **2005**, *4*, 366.

[13] C. K. Chan, H. Peng, G. Liu, K. McIlwrath, X. F. Zhang, R. A. Huggins, Y. Cui, *Nat. Nanotech.* **2008**, *3*, 31.

[14] A. Magasinski, P. Dixon, B. Hertzberg, A. Kvit, J. Ayala, G. Yushin, *Nat. Mater.* **2010**, *9*, 353.

[15] H. Wu, G. Chan, J. W. Choi, I. Ryu, Y. Yao, M. T. McDowell, S. W. Lee, A. Jackson, Y. Yang, L. Hu, Y. Cui, *Nat. Nanotech.* **2012**, *7*, 310.

[16] N. Liu, Z. Lu, J. Zhao, M. T. McDowell, H. W. Lee, W. Zhao, Y. Cui, *Nat. Nanotech.* **2014**, *9*, 187.

[17] J. Lu, Z. Chen, Z. Ma, F. Pan, L. A. Curtiss, K. Amine, *Nat. Nanotech.* **2016**, 11, 1031.

[18] S. Zhao, K. Yan, P. Munroe, B. Sun, G. Wang, *Adv. Energy Mater.* **2019**, *9*, 1803757.

[19] M. Qin, W. Ren, J. Meng, X. Wang, X. Yao, Y. Ke, Q. Li, L. Mai, *ACS Sustain. Chem. Eng.* **2019**, *7*, 11564.

[20] W. Luo, J. -J. Gaumet, P. Magri, S. Diliberto, F. Li, P. Franchetti, J. Ghanbaja, L. Mai, *J. Energy Chem.* **2019**, *30*, 27.

[21] S. Zhao, B. Sun, K. Yan, J. Zhang, C. Wang, G. Wang, *ACS Appl. Mater. Interfaces* **2018**, *10*, 332360.

[22] M. Winter and J. O. Besenhard, *Electrochim. Acta* **1999**, *45*, 31.

[23] U. Kasavajjula, C. Wang, A. J. Appleby, *J. Power Sources* **2007**, *163*, 1003.

[24] Y. Yu, L. Gu, C. Zhu, P. A. van Aken, J. Maier, *J. Am. Chem. Soc.* **2009**, *131*, 15984.

[25] H. Tian, F. Xin, X. Wang, W. He, W. Han, *J. Materiomics* **2015**, *1*, 153.

[26] H. Gao, L. Xiao, I. Pluemel, G.-L. Xu, Y. Ren, X. Zuo, Y. Liu, C. Schulz, H. Wiggers, K. Amine, Z. Chen, *Nano Lett.* **2017**, *17*, 1512.

[27] Q. Pang, A. Shyamsunder, B. Narayanan, C. Y. Kwok, L. A. Curtiss, L. F. Nazar, *Nat. Energy* **2018**, *3*, 783.

[28] J. Zheng, J. A. Lochala, A. Kwok, Z. D. Deng, J. Xiao, *Adv. Sci.* **2017**, *4*, 1700032.

[29] S. Jurng, Z. L. Brown, J. Kim, B. L. Lucht, *Energy Environ. Sci.* **2018**, *11*, 2600.

[30] Z. Zeng, V. Murugesan, K. S. Han, X. Jiang, Y. Cao, L. Xiao, X. Ai, H. Yang, J.-G. Zhang, M. L. Sushko, J. Liu, *Nat. Energy* **2018**, *3*, 674.

[31] T. Jaumann, J. Balach, U. Langklotz, V. Sauchuk, M. Fritsch, A. Michaelis, V. Teltevskij, D. Mikhailova, S. Oswald, M. Klose, G. Stephani, R. Hauser, J. Eckert, L. Giebeler, *Energy Storage Mater.* **2017**, *6*, 26.

[32] J. G. Han, J. B. Lee, A. Cha, T. K. Lee, W. Cho, S. Chae, S. J. Kang, S. K. Kwak, J. Cho, S. Y. Hong, N. S. Choi, *Energy Environ. Sci.* **2018**, *11*, 1552.

[33] Z. Y. Zhou, N. Tian, J. T. Li, I. Broadwell, S. G. Sun, *Chem. Soc. Rev.* **2011**, *40*, 4167.

[34] X. H. Liu, S. Huang, S. T. Picraux, J. Li, T. Zhu, J. Y. Huang, *Nano Lett.* **2011**, *11*, 3991.

[35] A. Darwiche, C. Marino, M. T. Sougrati, B. Fraisse, L. Stievano, L. Monconduit, *J. Am. Chem. Soc.* **2012**, *134*, 20805.

[36] M. He, K. Kravchyk, M. Walter, M. V. Kovalenko, *Nano Lett.* **2014**, *14*, 1255.

[37] J. Rohrer and P. Kaghazchi, *Chemphyschem* **2014**, *15*, 3950.

[38] E. Markevich, G. Salitra, D. Aurbach, *ACS Energy Lett.* **2017**, *2*, 1337.

[39] Z.-S. Wu, L. Xue, W. Ren, F. Li, L. Wen, H. M. Cheng, *Adv. Funct. Mater.* **2012**, *22*, 3290.

[40] L. Zhang, K. Zhang, Z. Shi, S. Zhang, *Langmuir* **2017**, *33*, 11164.

[41] Z. Zhu, Y. Tang, Z. Lv, J. Wei, Y. Zhang, R. Wang, W. Zhang, H. Xia, M. Ge, X. Chen, *Angew. Chem. Int. Ed.* **2018**, *57*, 3656.

[42] W. Liang, H. Yang, F. Fan, Y. Liu, X. H. Liu, J. Y. Huang, T. Zhu, S. Zhang, *ACS Nano* **2013**, *7*, 3427.

[43] Y. Liu, X. H. Liu, B. M. Nguyen, J. Yoo, J. P. Sullivan, S. T. Picraux, J. Y. Huang, S. A. Dayeh, *Nano Lett.* **2013**, *13*, 4876.

[44] L. Y. Lim, N. Liu, Y. Cui, M. F. Toney, *Chem. Mater.* **2014**, *26*, 3739.

[45] K. E. Silberstein, M. A. Lowe, B. Richards, J. Gao, T. Hanrath, H. D. Abruna, *Langmuir* **2015**, *31*, 2028.

[46] C. K. Chan, X. F. Zhang, Y. Cui, *Nano Lett.* **2008**, *8*, 307.

[47] N. K. Mahenderkar, Y.-C. Liu, J. A. Koza, J. A. Switzer, *ACS Nano* **2014**, *8*, 9524.

[48] P. Verma, P. Maire, P. Novak, *Electrochim. Acta* **2010**, *55*, 6332.

[49] X. Fan, X. Ji, F. Han, J. Yue, J. Chen, L. Chen, T. Deng, J. Jiang, C. Wang, *Sci. Adv.* **2018**, *4*, eaau9245.

[50] X. Zhou, T. Li, Y. Cui, Y. Fu, Y. Liu, L. Zhu, *ACS Appl. Mater. Interfaces* **2019**, *11*, 1733.

[51] S. Shen, Y. Hong, F. Zhu, Z. Cao, Y. Li, F. Ke, J. Fan, L. Zhou, L. Wu, P. Dai, M. Cai, L. Huang, Z. Zhou, J. Li, Q. Wu, S. Sun, *ACS Appl. Mater. Interfaces* **2018**, *10*, 12666.

[52] J. P. Perdew, K. Burke, M. Ernzerhof, *Phys. Rev. Lett.* **1996**, *77*, 3865.

[53] P. Giannozzi, S. Baroni, N. Bonini, M. Calandra, R. Car, C. Cavazzoni, D. Ceresoli, G. L. Chiarotti, M. Cococcioni, I. Dabo, A. Dal Corso, S. de Gironcoli, S. Fabris, G. Fratesi, R. Gebauer, U. Gerstmann, C. Gougoussis, A. Kokalj, M. Lazzeri, L. Martin-Samos, N. Marzari, F. Mauri, R. Mazzarello, S. Paolini, A. Pasquarello, L. Paulatto, C. Sbraccia, S. Scandolo, G. Sclauzero, A. P. Seitsonen, A. Smogunov, P. Umari, R. M. Wentzcovitch, *J. Phys. Condens. Matter*. **2009**, *21*, 395502.

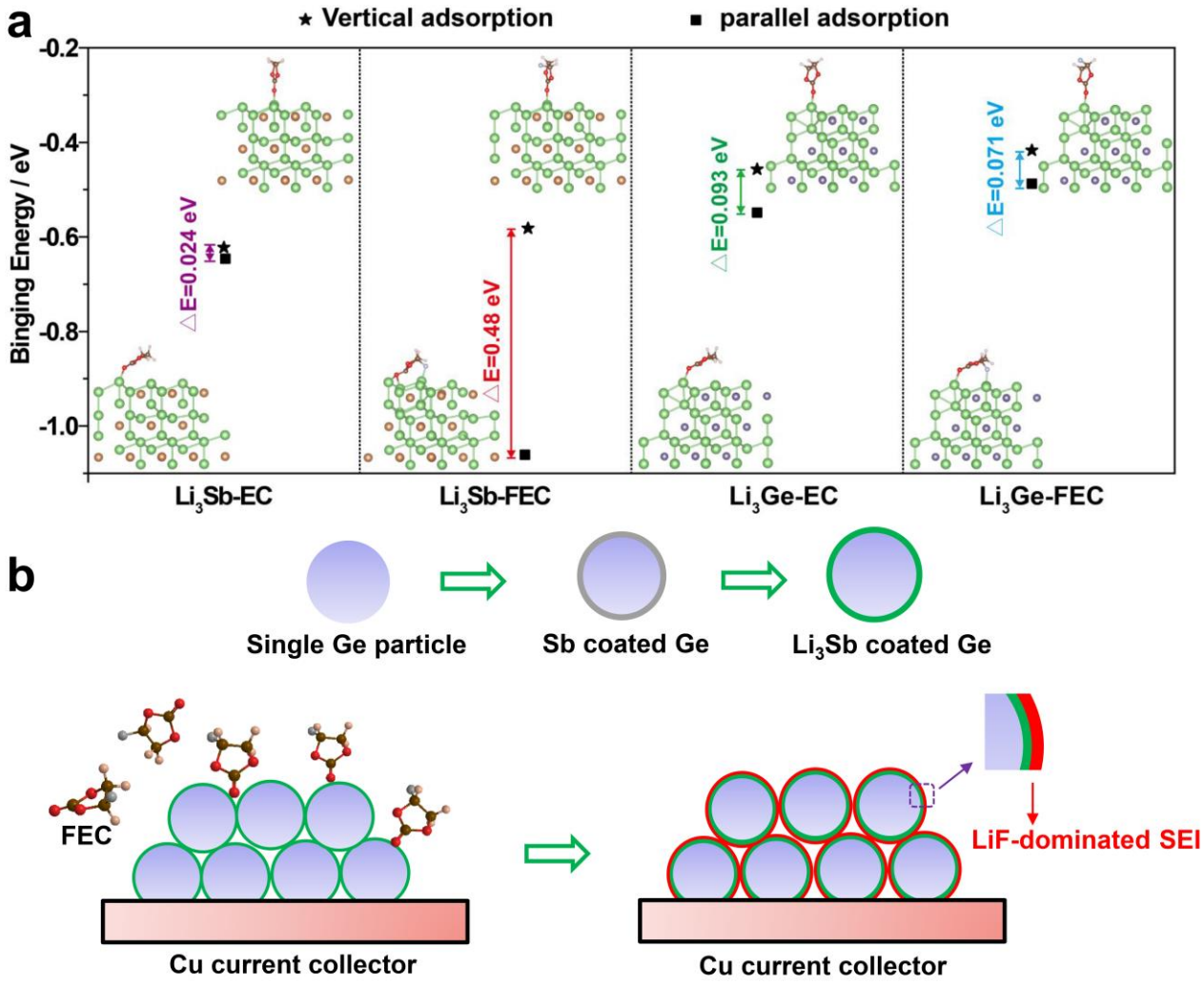

Figure 1. a) DFT calculation on the binding energy of EC and FEC molecules on the Li_3Sb (111) and Li_3Ge (111) surfaces at vertical and parallel adsorption. Brown, blue, green, and red represent Sb, Ge, Li, and O, respectively. b) Schematic of the function of the ultraconformal Sb layer during discharge.

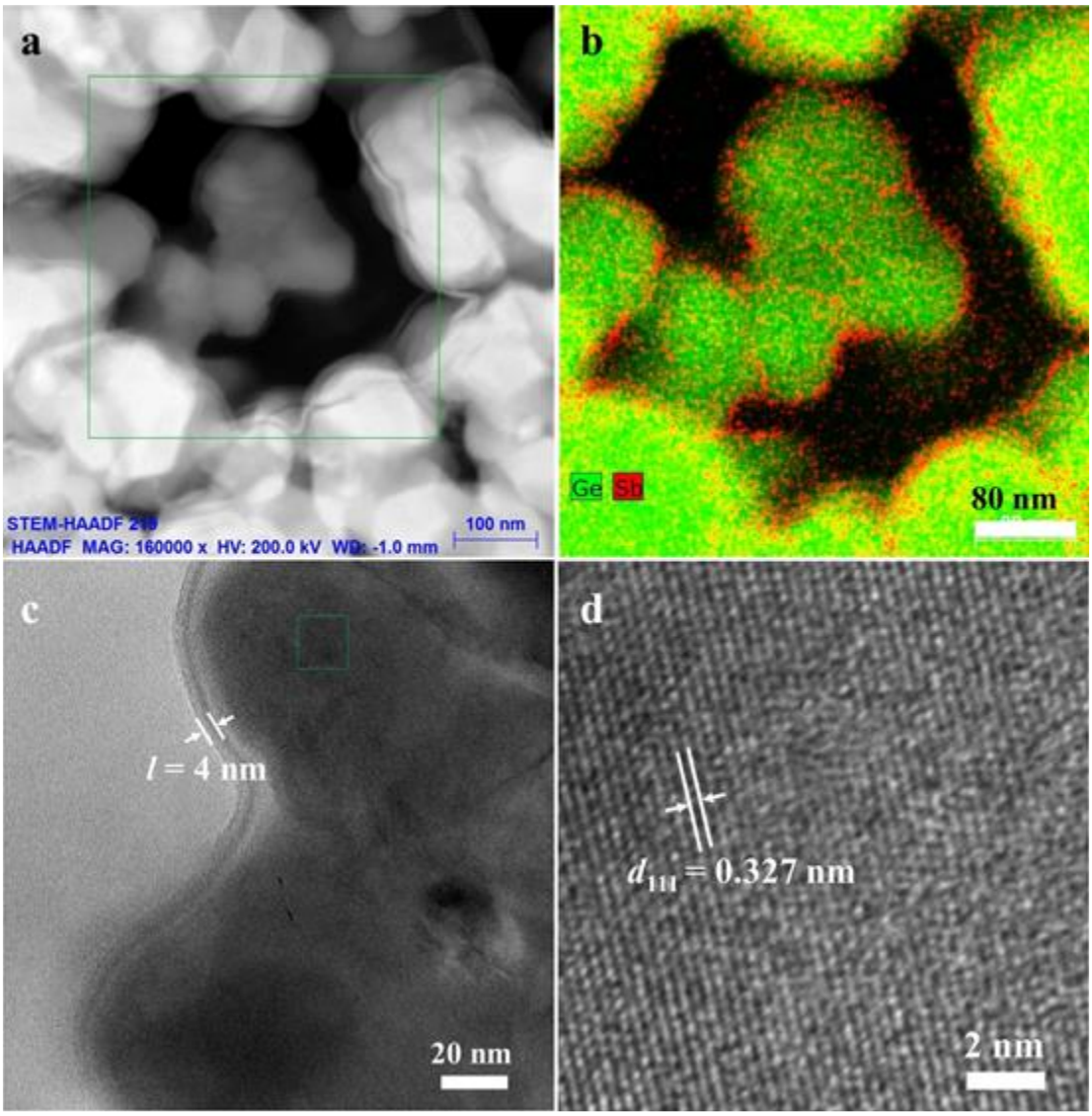

Figure 2. a) HAADF-STEM image of the inner surface and b) corresponding elemental mapping of Sb-coated-porous Ge, c) TEM and d) HR-TEM images of Sb-coated-porous Ge.

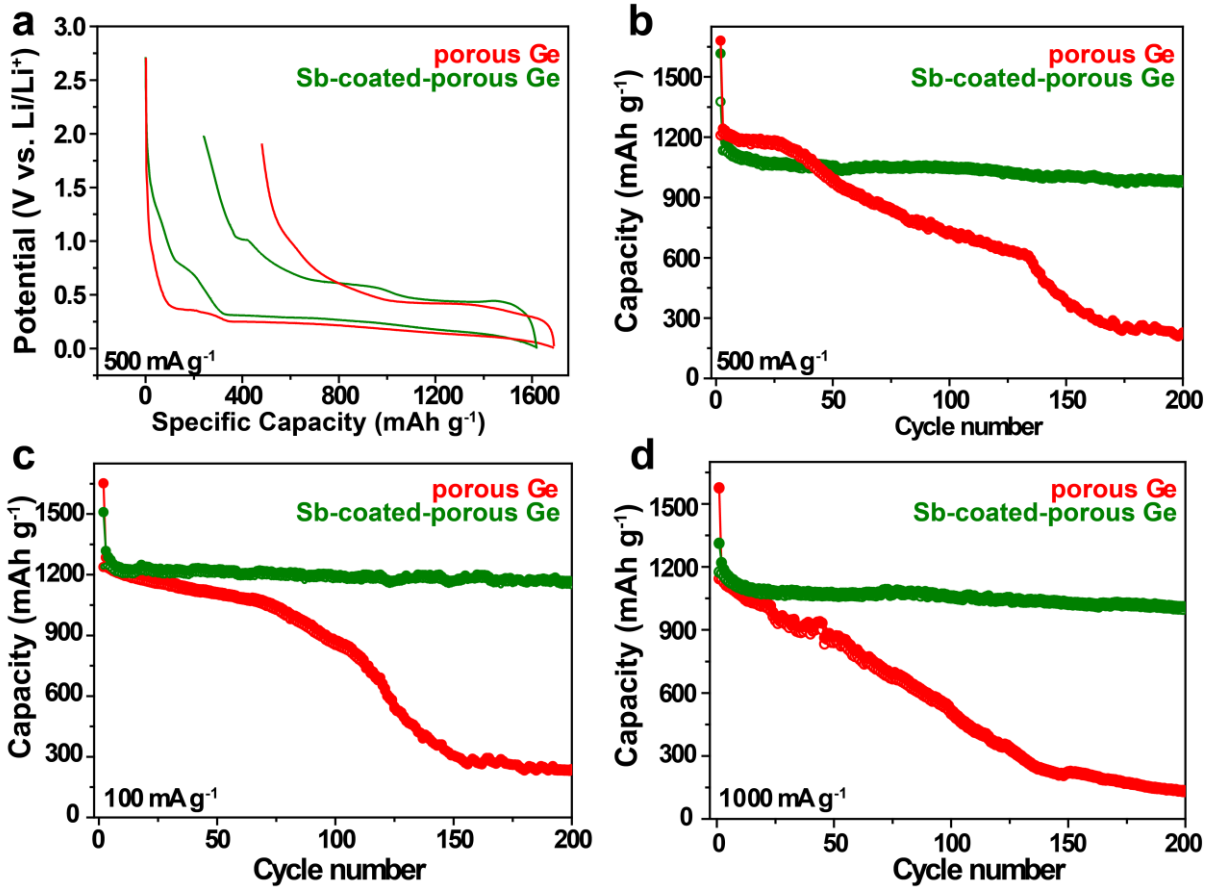

Figure 3. a) Initial potential profiles of Sb-coated and uncoated porous Ge electrodes in the voltage range of 0.01–2.0 V vs. Li/Li^+ at current density of 500 mA g^{-1}. b, c, and d) Cycling performances of Sb-coated and uncoated porous Ge electrodes at current densities of 500 mA g^{-1}, 100 mA g^{-1}, and 1000 mA g^{-1}.

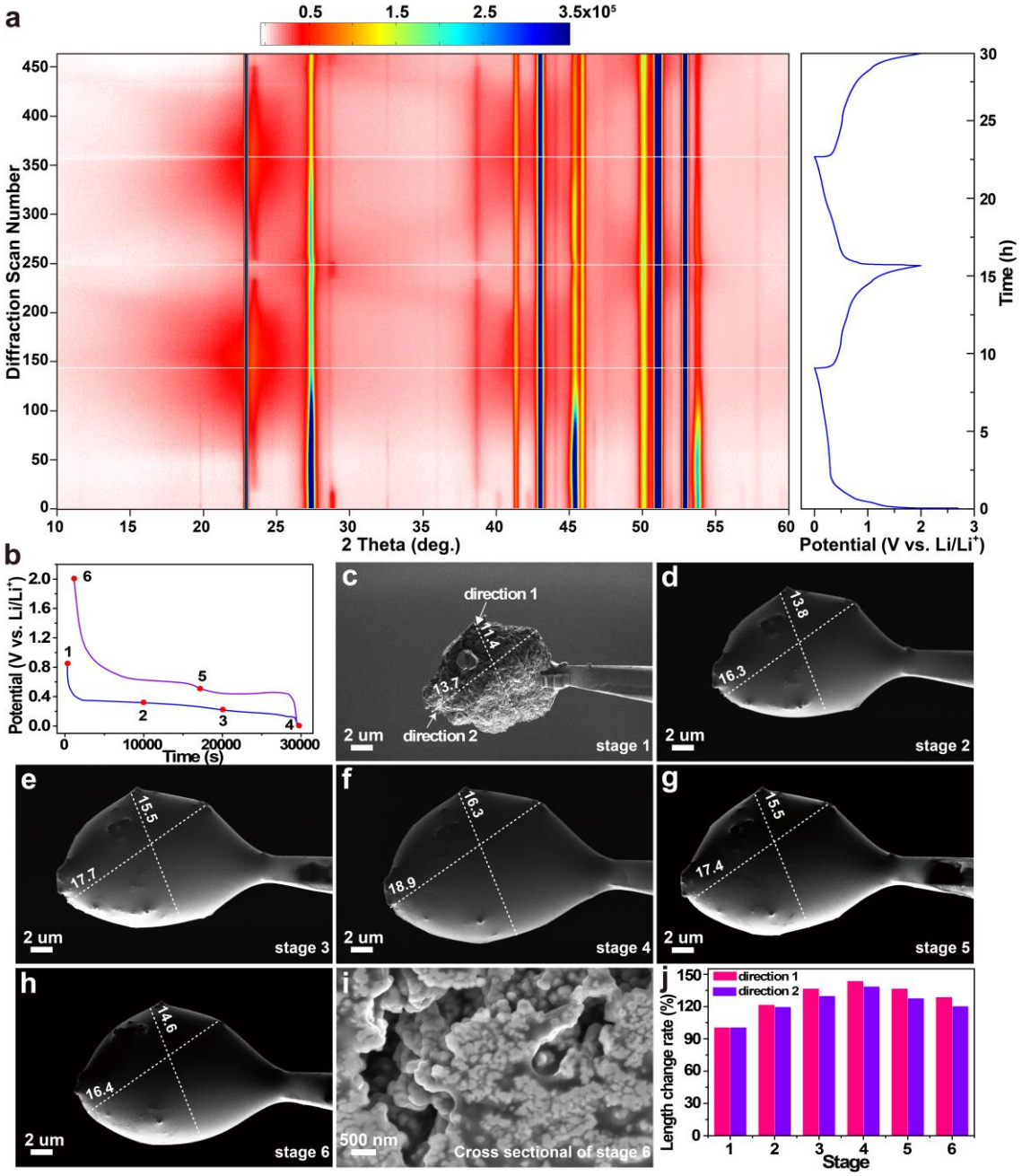

Figure 4. a) First two-cycle discharge-charge curves and the corresponding *in situ* PXRD patterns of Sb-coated Ge electrode at 150 mA g^{-1}. b-h) The initial lithiation/delithiation curves and the corresponding *in situ* SEM images of a single Sb-coated-Ge porous particle. i) Cross-sectional SEM image of stage 6. j) Length changes of the Sb-coated-Ge porous particle in different stages. We defined the length as 100% in two directions at stage 1.

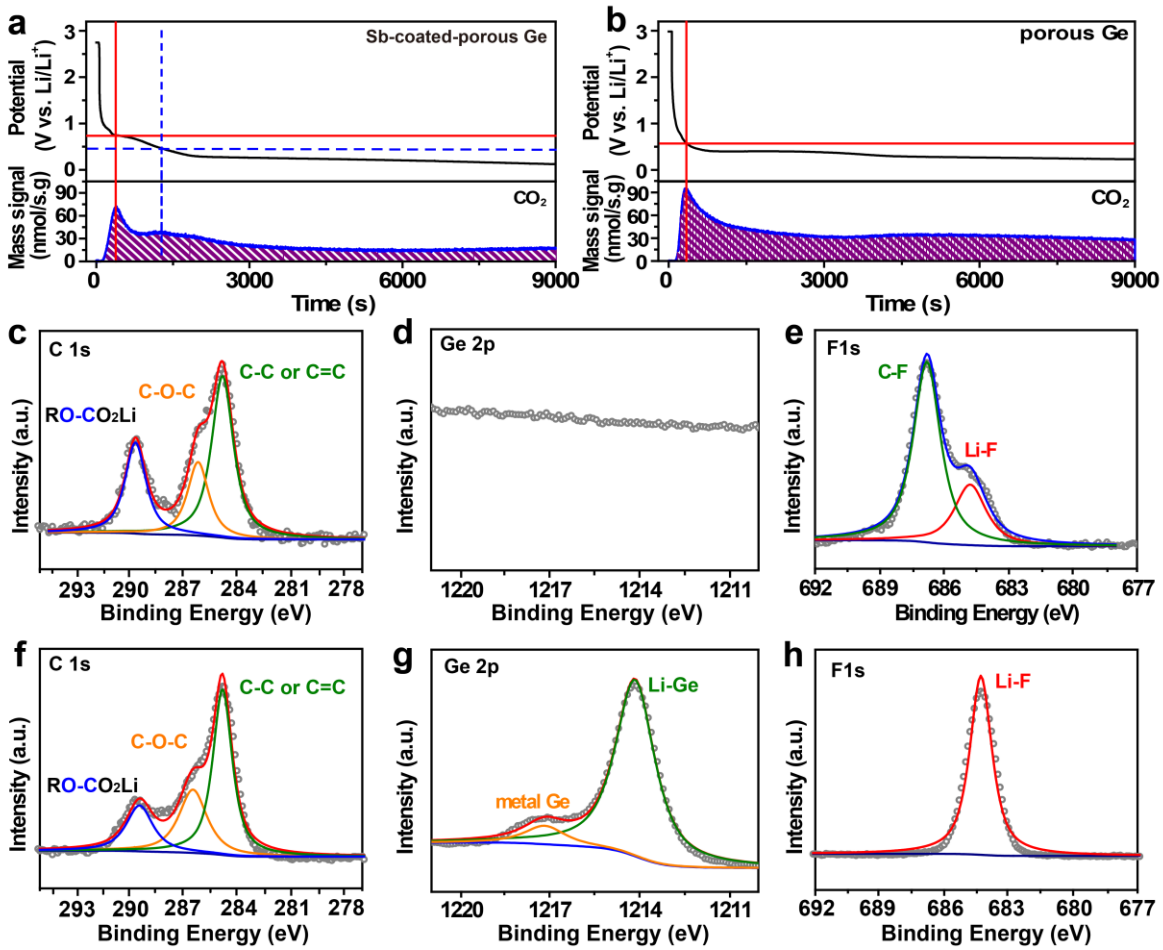

Figure 5. Plots of CO_2 (m/z = 44) evolution of a) Sb-coated porous Ge and b) uncoated porous Ge electrodes for the first 150 min during discharge. XPS analysis of c, f) carbon, d, g) germanium, and e, h) fluorine at the initial full discharge for these electrodes.

A simple approach to favorable solid-electrolyte interphase (SEI) design for alloy-based anodes is proposed by surface coating of an ultraconformal Sb layer. This strategy can guide and regulate the catalytic decomposition of electrolyte components, leading to the formation of robust, thin and dense LiF-dominated SEI. Hence, both cycle stability and initial coulombic efficiency of alloy-based anodes are remarkably improved.

Keyword: Antimony, Anode materials, Batteries, Solid electrolyte interphase, Catalytic decomposition

Bing-Qing Xiong, Xinwei Zhou, Gui-Liang Xu,* Yuzi Liu, Likun Zhu, Youcheng Hu, Shou-Yu Shen, Yu-Hao Hong, Si-Cheng Wan, Xiao-Chen Liu, Xiang Liu, Shengli Chen, Ling Huang, Shi-Gang Sun, Khalil Amine,* and Fu-Sheng Ke*

Boosting Superior Lithium Storage Performance of Alloy-based Anode Materials via Ultraconformal Sb Coating derived Favorable Solid-electrolyte Interphase

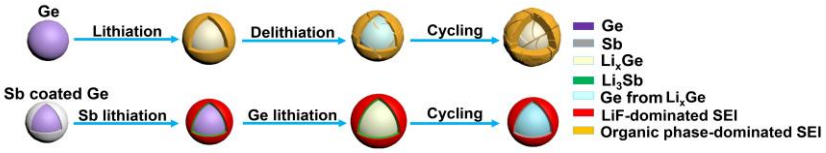

Copyright WILEY-VCH Verlag GmbH & Co. KGaA, 69469 Weinheim, Germany, 2016.

Supporting Information

Boosting Superior Lithium Storage Performance of Alloy-based Anode Materials via Ultraconformal Sb Coating derived Favorable Solid-electrolyte Interphase

Bing-Qing Xiong, Xinwei Zhou, Gui-Liang Xu, Yuzi Liu, Likun Zhu, Youcheng Hu, Shou-Yu Shen, Yu-Hao Hong, Si-Cheng Wan, Xiao-Chen Liu, Xiang Liu, Shengli Chen, Ling Huang, Shi-Gang Sun, Khalil Amine,* and Fu-Sheng Ke**

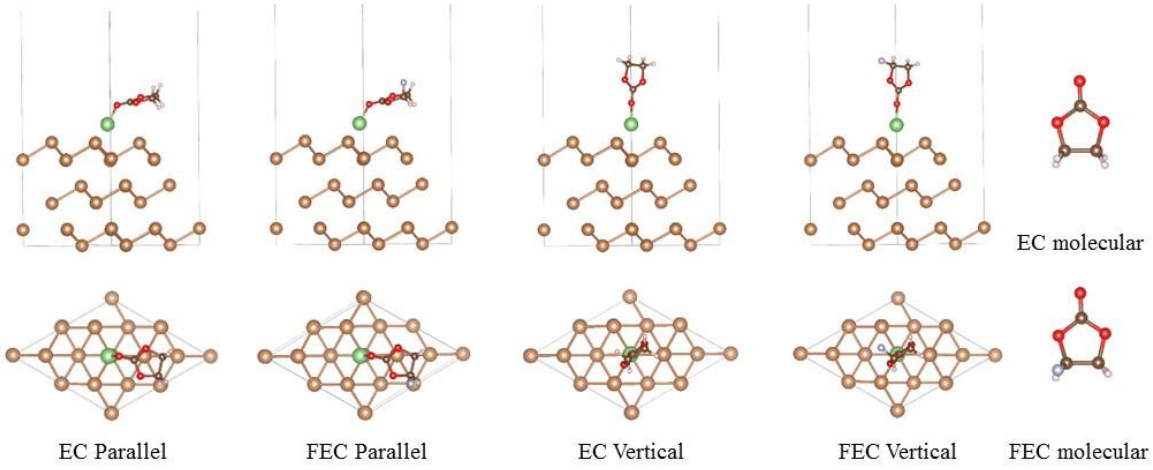

Figure S1. Main and top view of configurations after parallel/vertical adsorbing of FEC/EC on Sb (111) surface with low Li concentration (Li : EC/FEC=1:1). Brown, green, and red represent Sb, Li, and O, respectively.

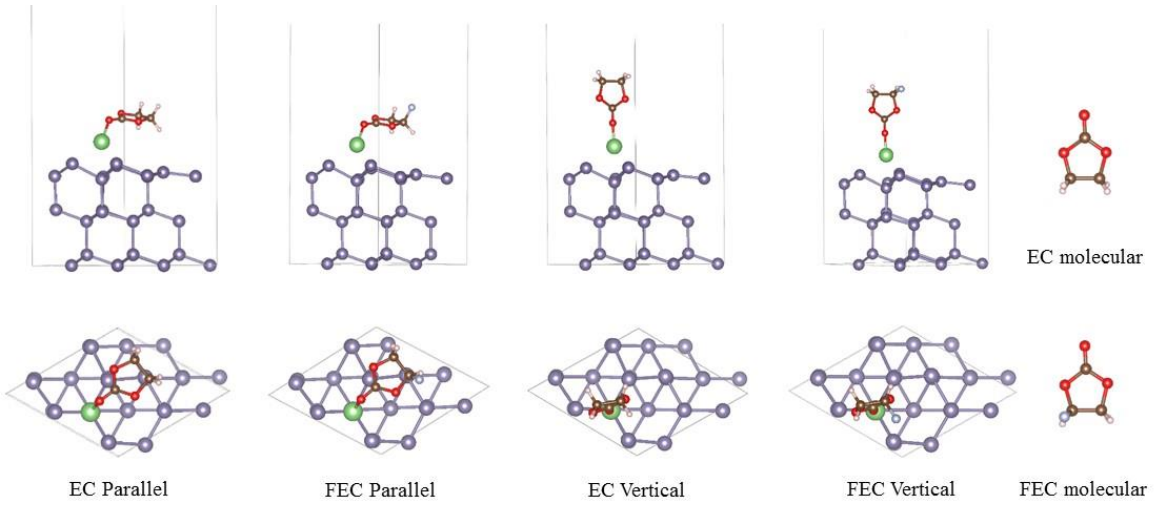

Figure S2. Main and top view of configurations after parallel/vertical adsorbing of FEC/EC on Ge (111) surface with low Li concentration (Li : EC/FEC=1:1). Green, blue, and red represent Li, Ge, and O, respectively.

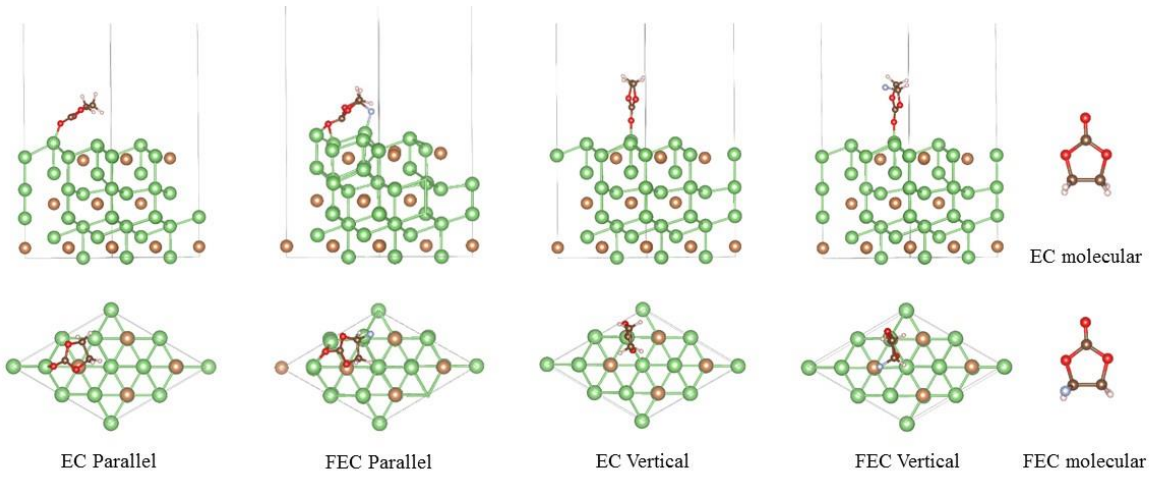

Figure S3. Main and top view of configurations after parallel/vertical adsorbing of FEC/EC on Li_3Sb (111) surface. Brown, green, and red represent Sb, Li, and O, respectively.

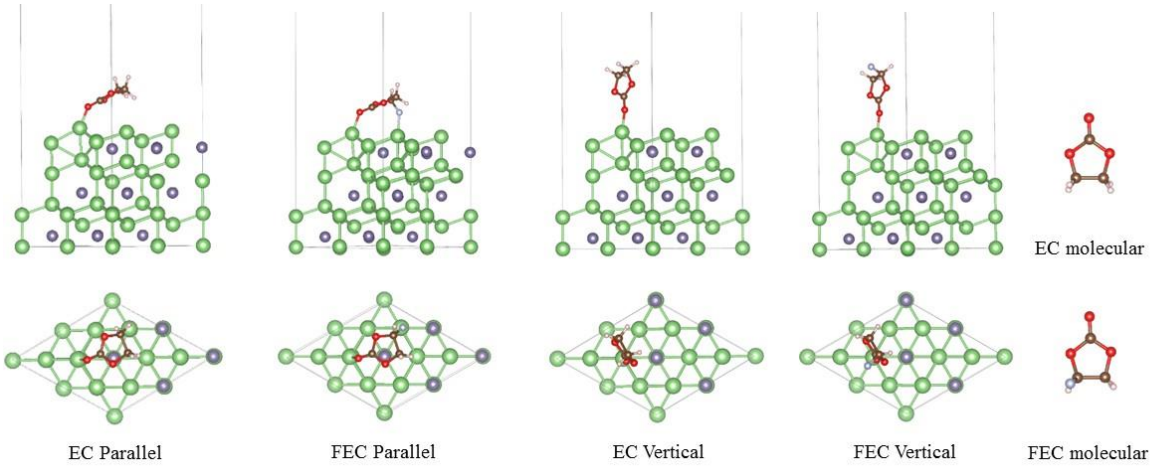

Figure S4. Main and top view of configurations after parallel/vertical adsorbing of FEC/EC on Li_3Ge (111) surface. Green, blue, and red represent Li, Ge, and O, respectively.

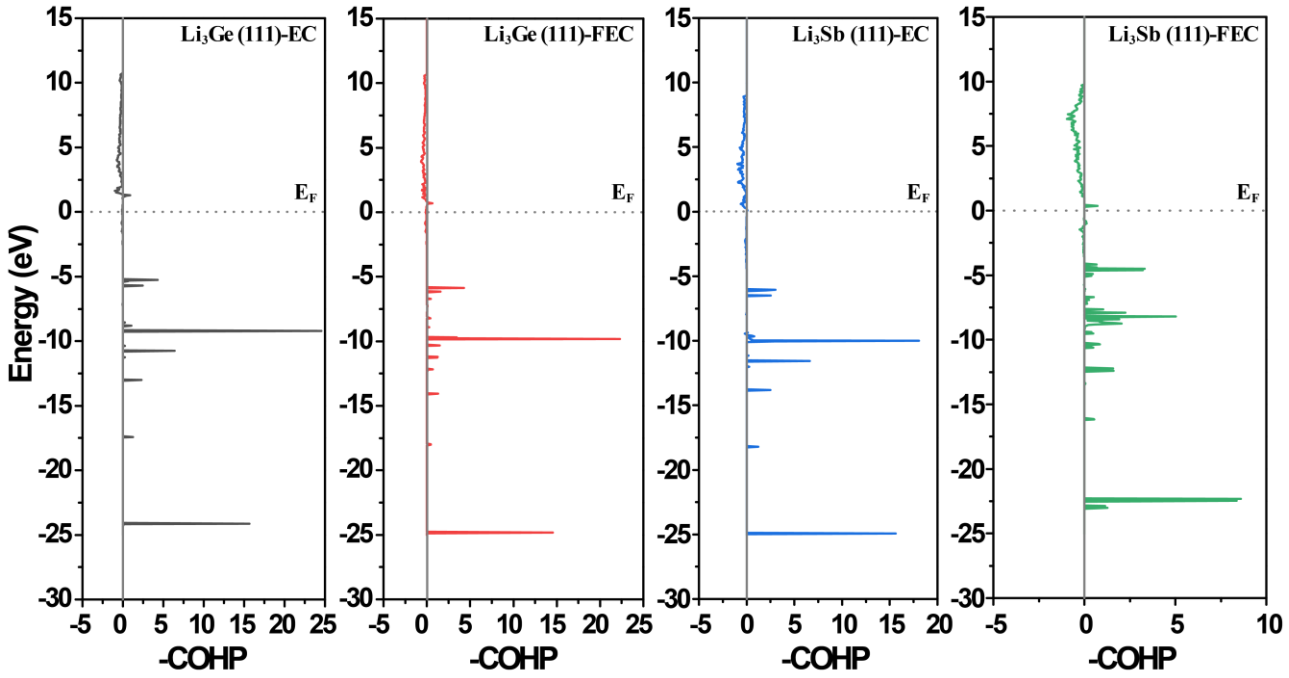

Figure S5. -COHP of Li-O bond between EC/FEC and Li_3Sb (111)/ Li_3Ge (111). Bonding states (positive, to the right) and antibonding states (negative, to the left).

According to the crystal orbital Hamilton populations (COHP), the bonding states is negative value and antibonding states is positive value, thus integrated COHP (ICOHP) could describe quantitatively the strength of bond in which more negative ICOHP value, more strength of bond.[1, 2] For Li_3Ge (111) surface, it is clearly observed that the Li-O bond (-1.57) of EC is higher than

that of Li-O (-1.43) and Li-F (-1.39) bonds of FEC, i.e. the adsorption of EC molecular on Li_3Ge (111) surface is much stronger than that of FEC molecular. For Li_3Sb (111) surface, a small difference (0.05) in ICOHP of Li-O bond between EC and FEC is observed, which means that the strength of Li-O bonds for the EC and FEC adsorbed on Li_3Sb (111) surface is almost same. Meanwhile, F atom of FEC is also bonded with Li atom of Li_3Sb (111) whose bond is more strong (ICOHP = -1.56), thus the adsorption of FEC on Li_3Sb (111) is stronger than the adsorption of EC on the Li_3Sb (111) surface. These results of COHP analysis are consistent with adsorption energy of DFT calculation.

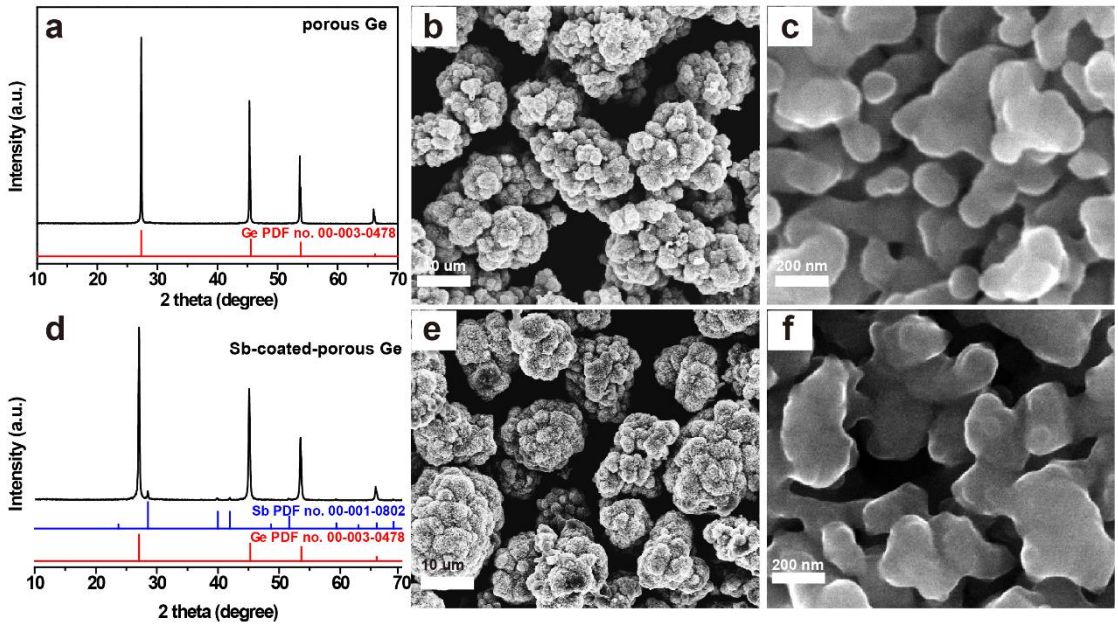

Figure S6. PXRD patterns, SEM images, and corresponding high-magnification images of porous Ge (a, b, c) and Sb-coated-porous Ge (d, e, f).

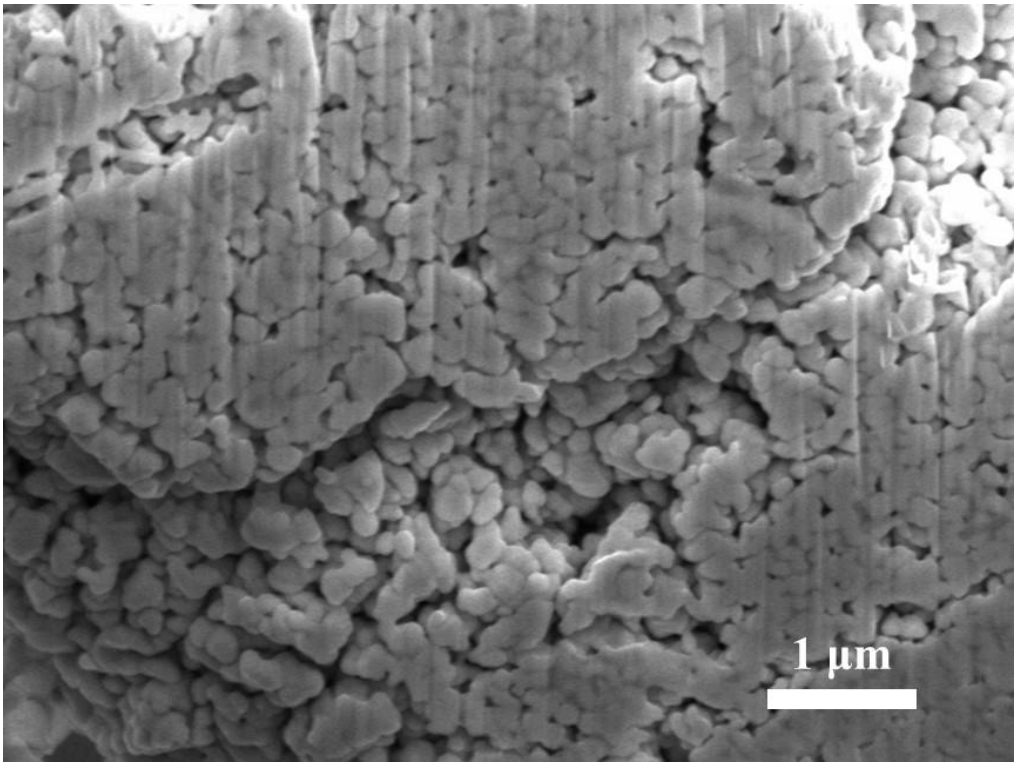

Figure S7. Cross-sectional SEM image of a single Sb-coated-porous Ge particle, which was cut by a focused ion beam.

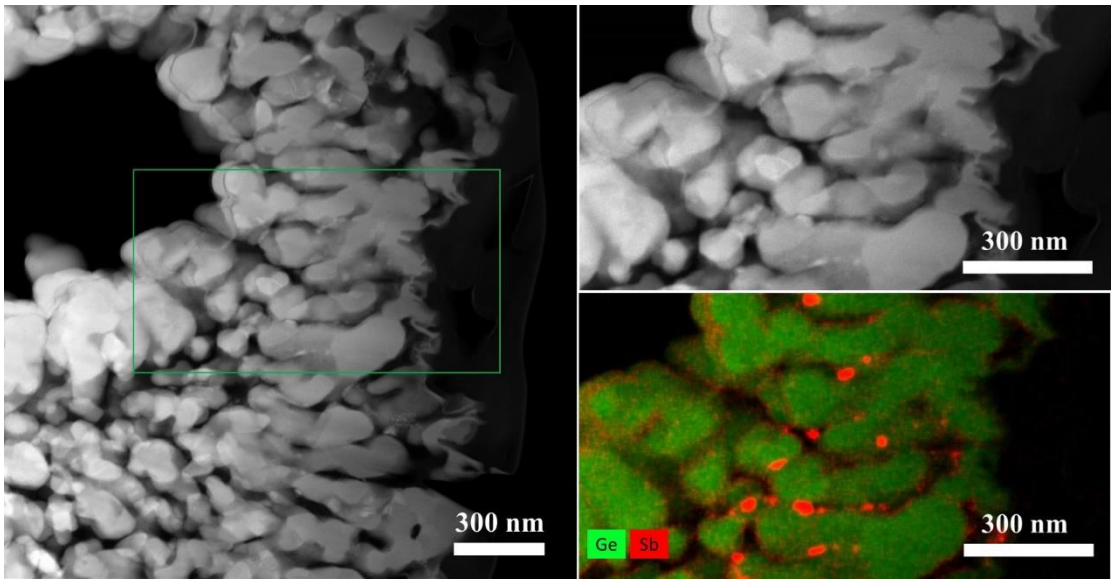

Figure S8. HAADF-TEM images of the outer surface of Sb-coated-porous Ge particles and XEDS elemental mapping of overlay of Ge vs. Sb.

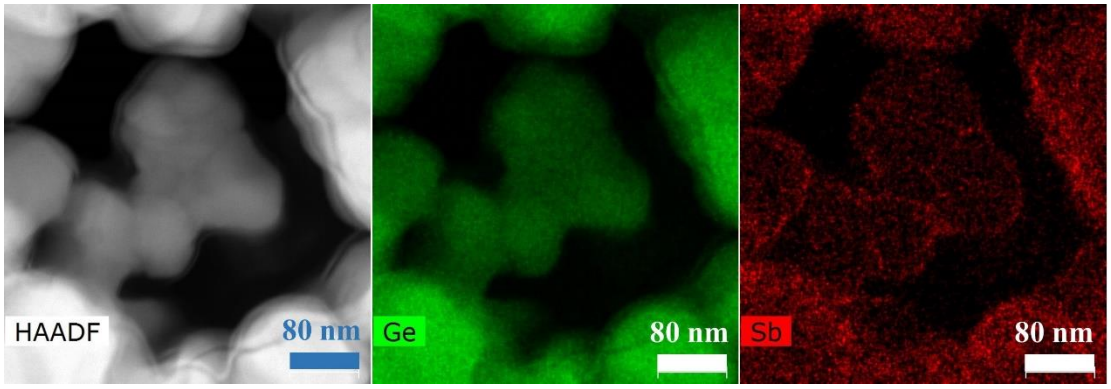

Figure S9. HAADF-TEM images of the inner surface of Sb-coated-porous Ge particles and XEDS elemental mapping of Ge and Sb.

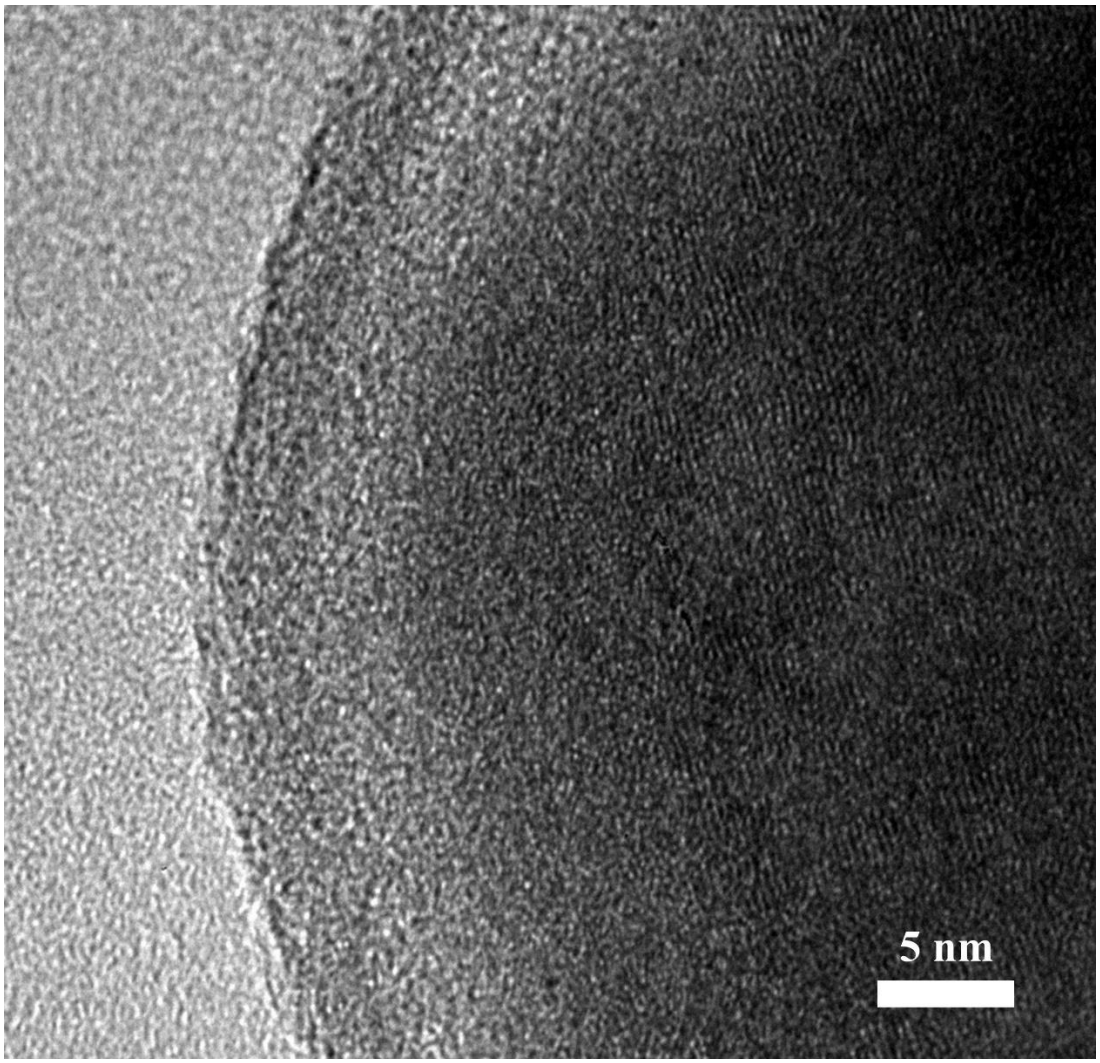

Figure S10. HR-TEM image of the edge of Sb-coated-porous Ge particle.

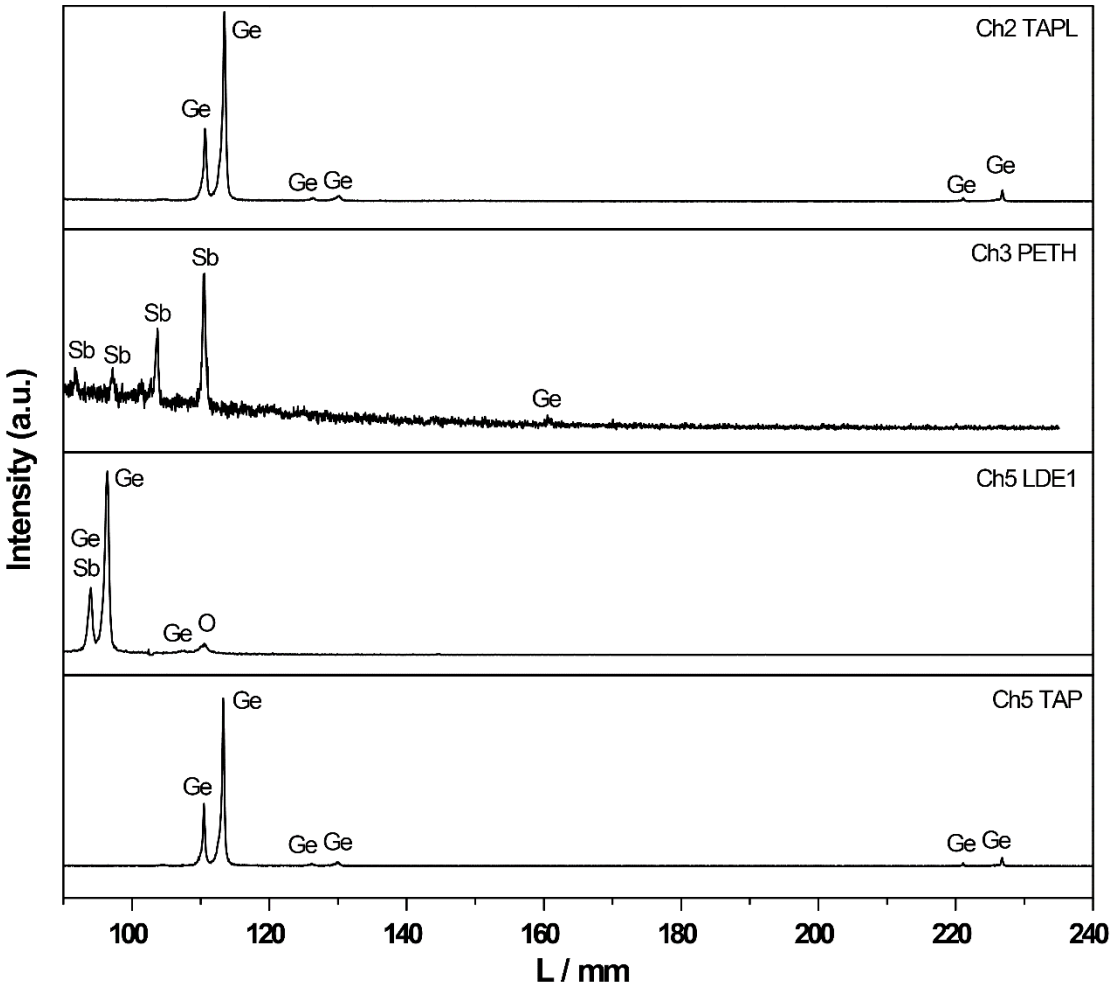

Figure S11. Electron probe micro-analyzer (EPMA) spectra of Sb-coated-porous Ge compound. According to the EPMA spectra, the content of Sb, O, and Ge is 4.5, 3.0, and 92.5 wt.%, respectively.

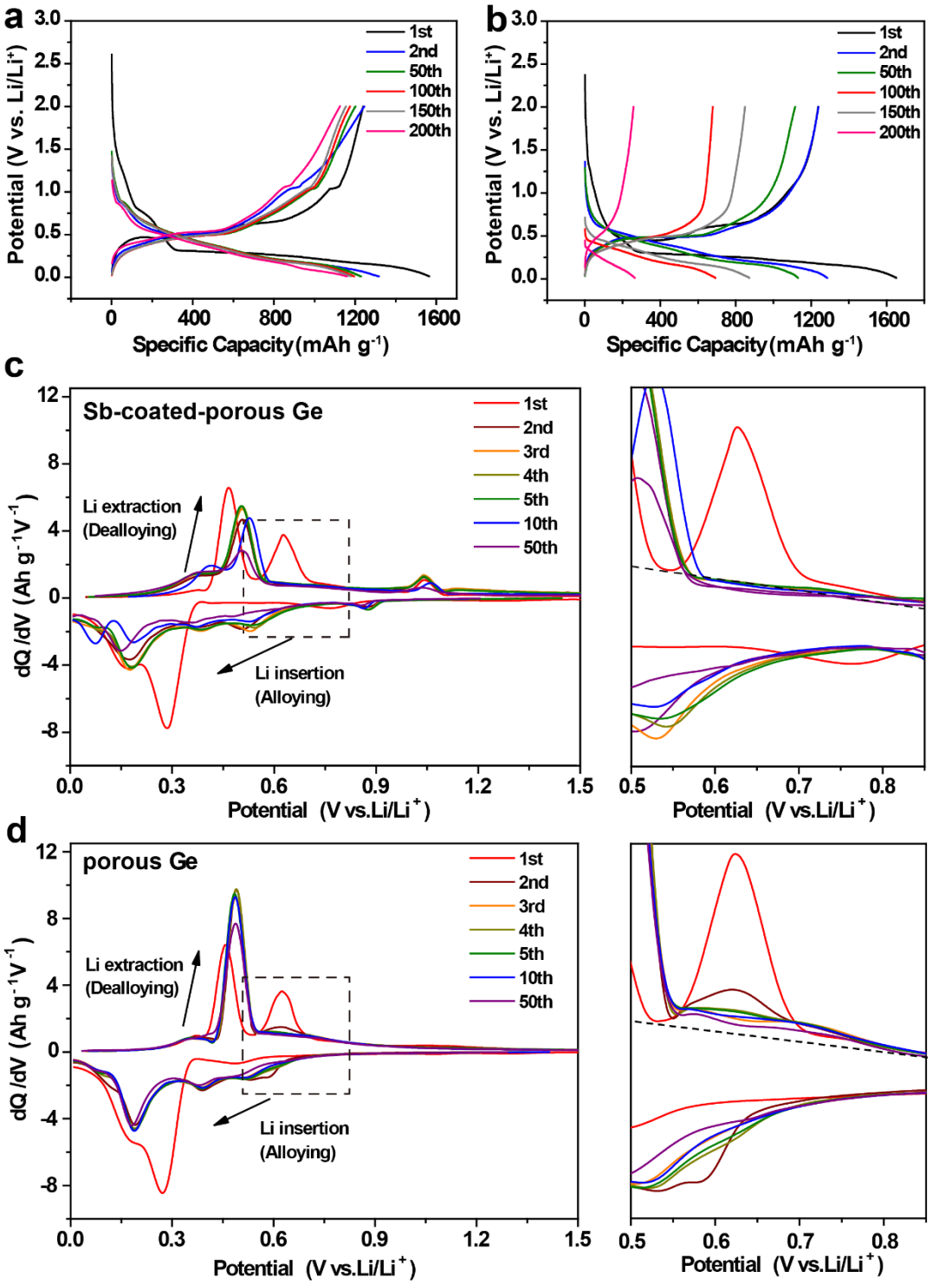

Figure S12. Voltage profiles of (**a**) Sb-coated-porous Ge and (**b**) porous Ge electrodes at current density of 500 mA g^{-1}, corresponding differential capacity plots of (**c**) Sb-coated-porous Ge and (**d**) porous Ge electrodes.

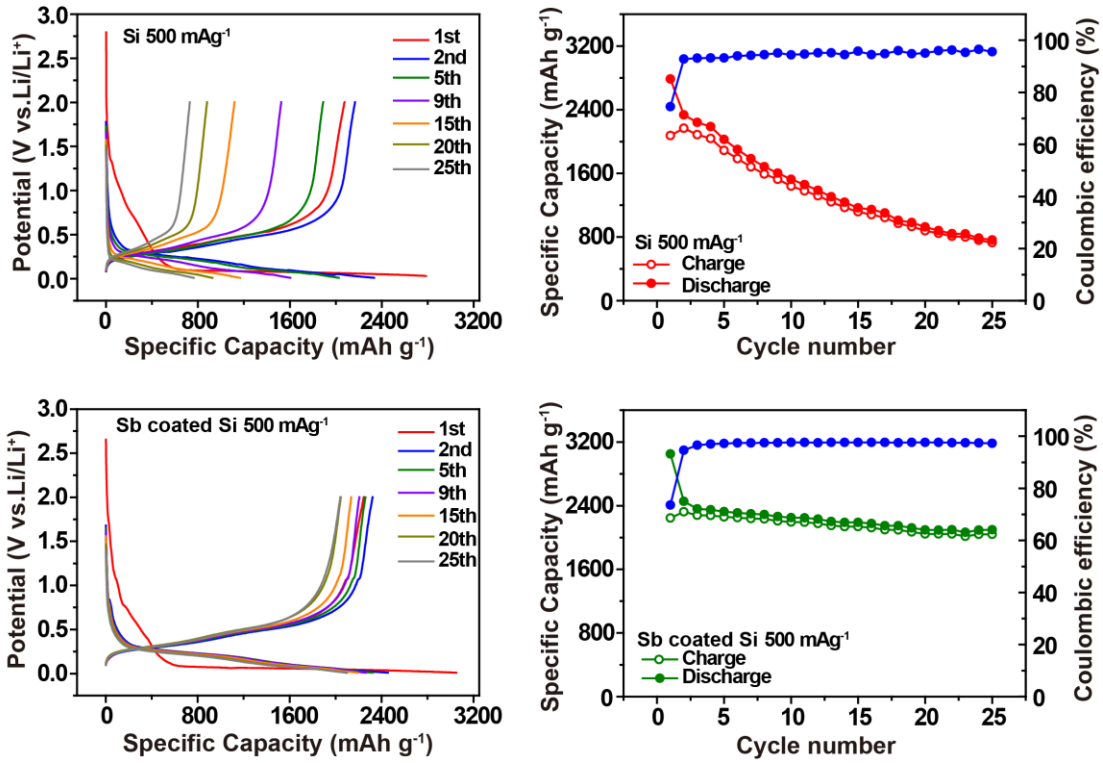

Figure S13. Voltage profiles and cycling performances of (a, b) Si and (c, d) Sb-coated Si electrodes.

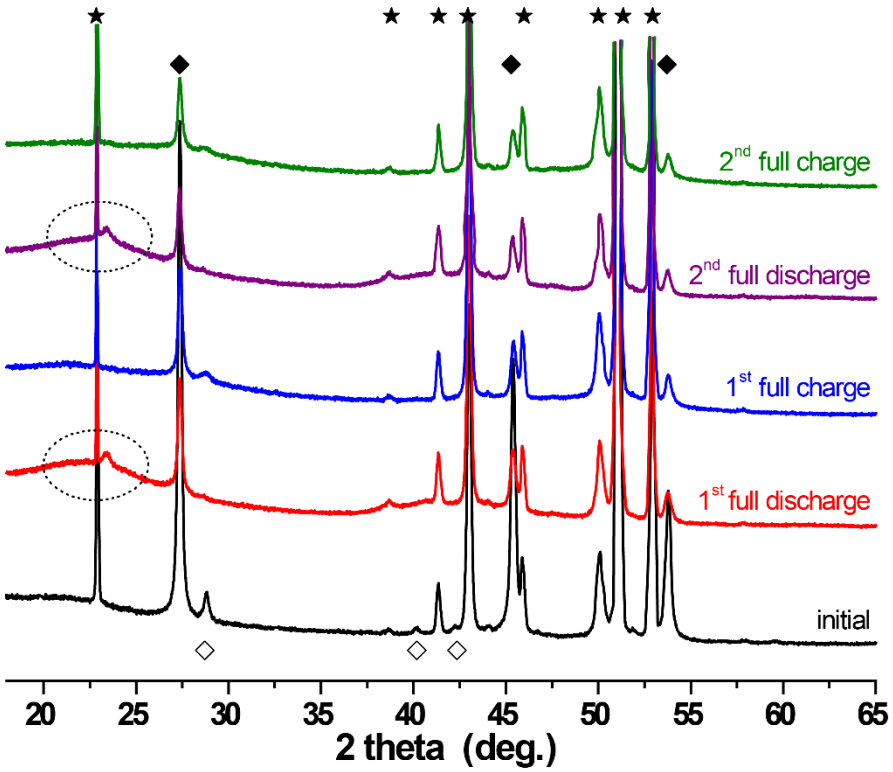

Figure S14. Discrete *in situ* XRD selected from Figure 3a. (★) BeO, Be, or substrate, (◆)Ge, (◇)Sb. The dashed regions are Li_3Sb and $Li_{15}Ge_4$.

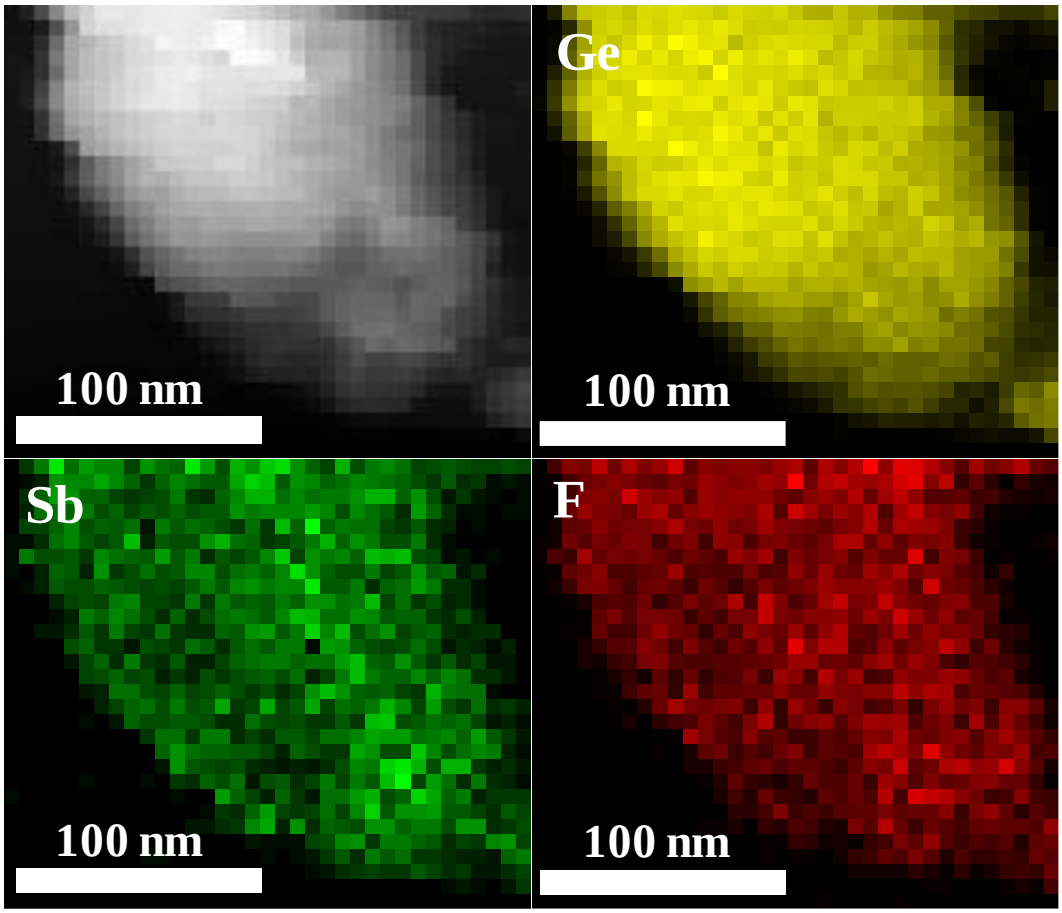

Figure S15. HAADF-STEM image and the corresponding elemental mapping of Ge, Sb and F of Sb-coated-porous Ge electrode after one cycle.

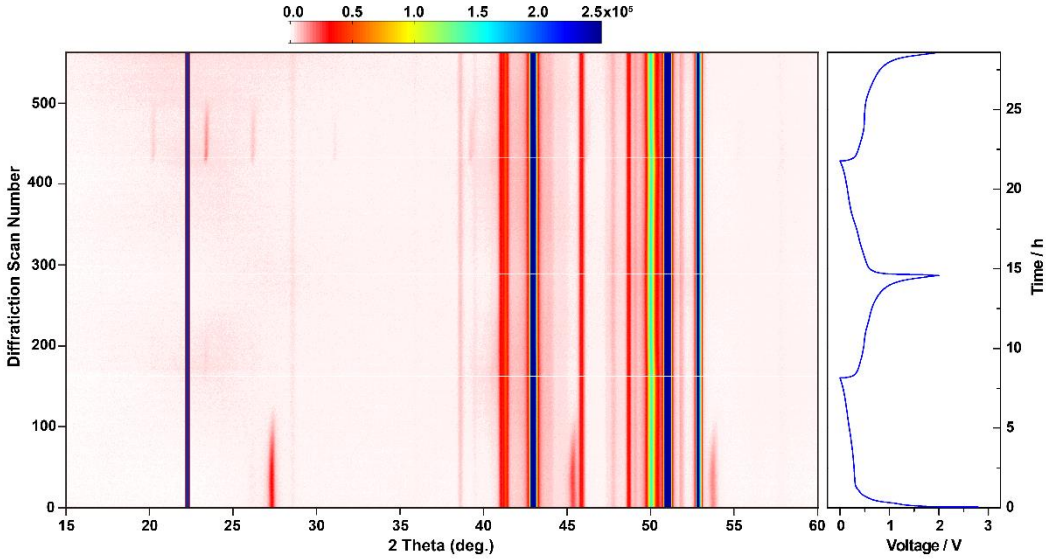

Figure S16. Discharge-charge curves for first two curves and the corresponding *in situ* XRD patterns of porous Ge electrode at 150 mA g^{-1}.

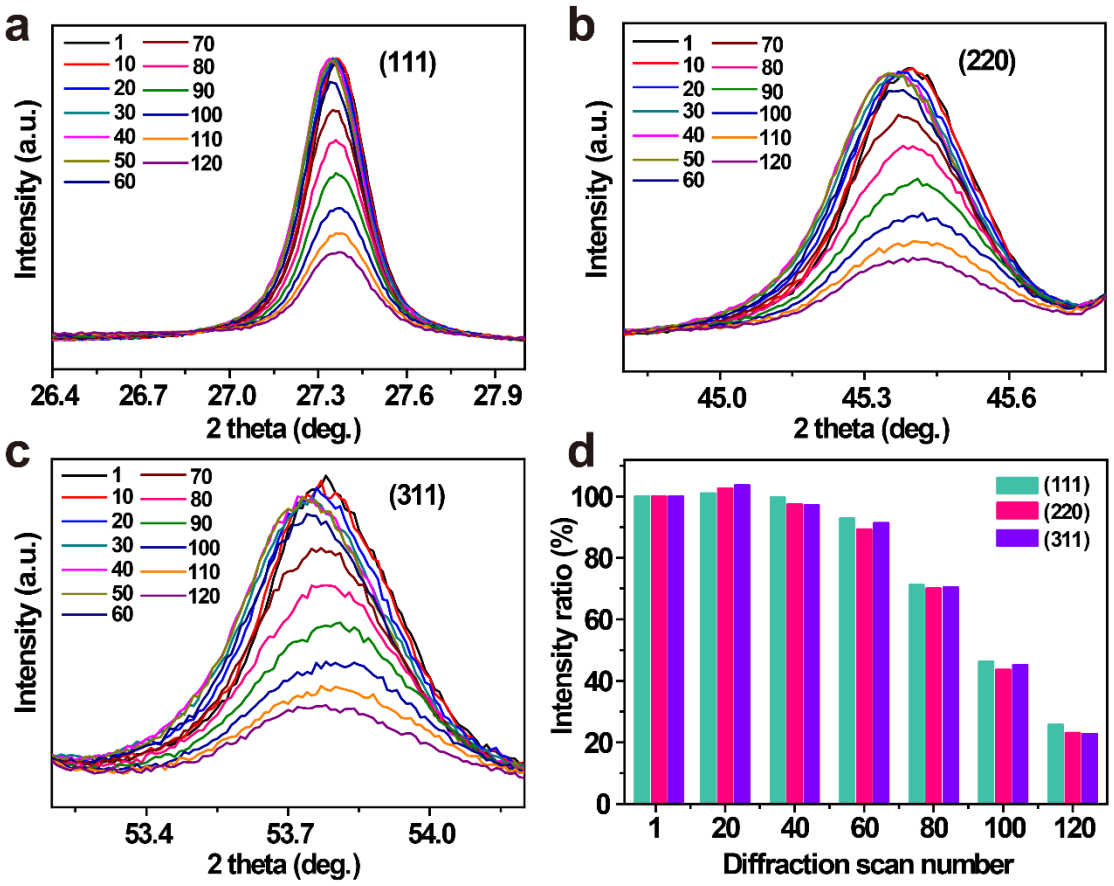

Figure S17. Selected XRD patterns during the first discharge of the Sb-coated-porous Ge: (a) (111), (b) (220), and (c) (311) reflection peaks. (d) Intensity of the three reflection peaks with scan number. We defined the intensity of (111), (220), and (311) peaks of the first diffraction scan as 100%.

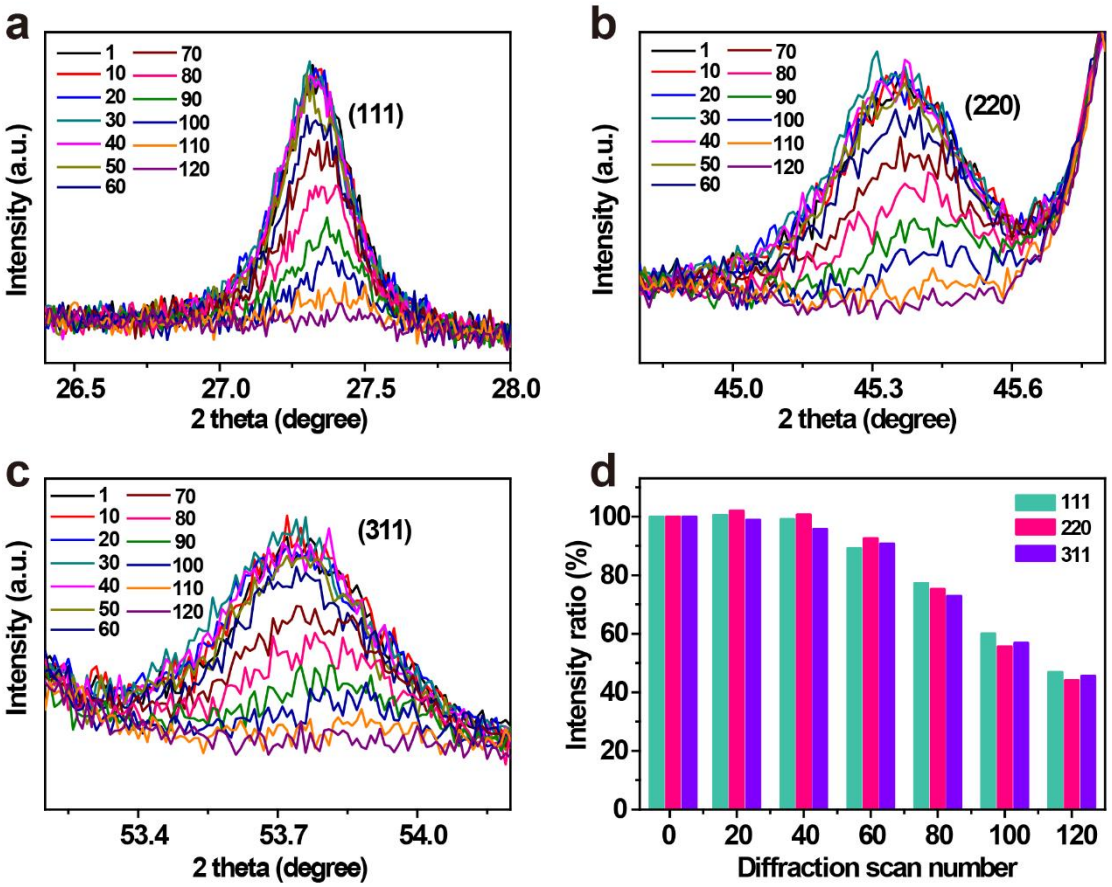

Figure S18. Selected XRD patterns during first discharge of the porous Ge: (a) (111), (b) (220), and (c) (311) reflection peaks. (d) Intensity of the three reflection peaks with scan number. We defined the intensity of (111), (220), and (311) peaks of the first diffraction scan as 100%.

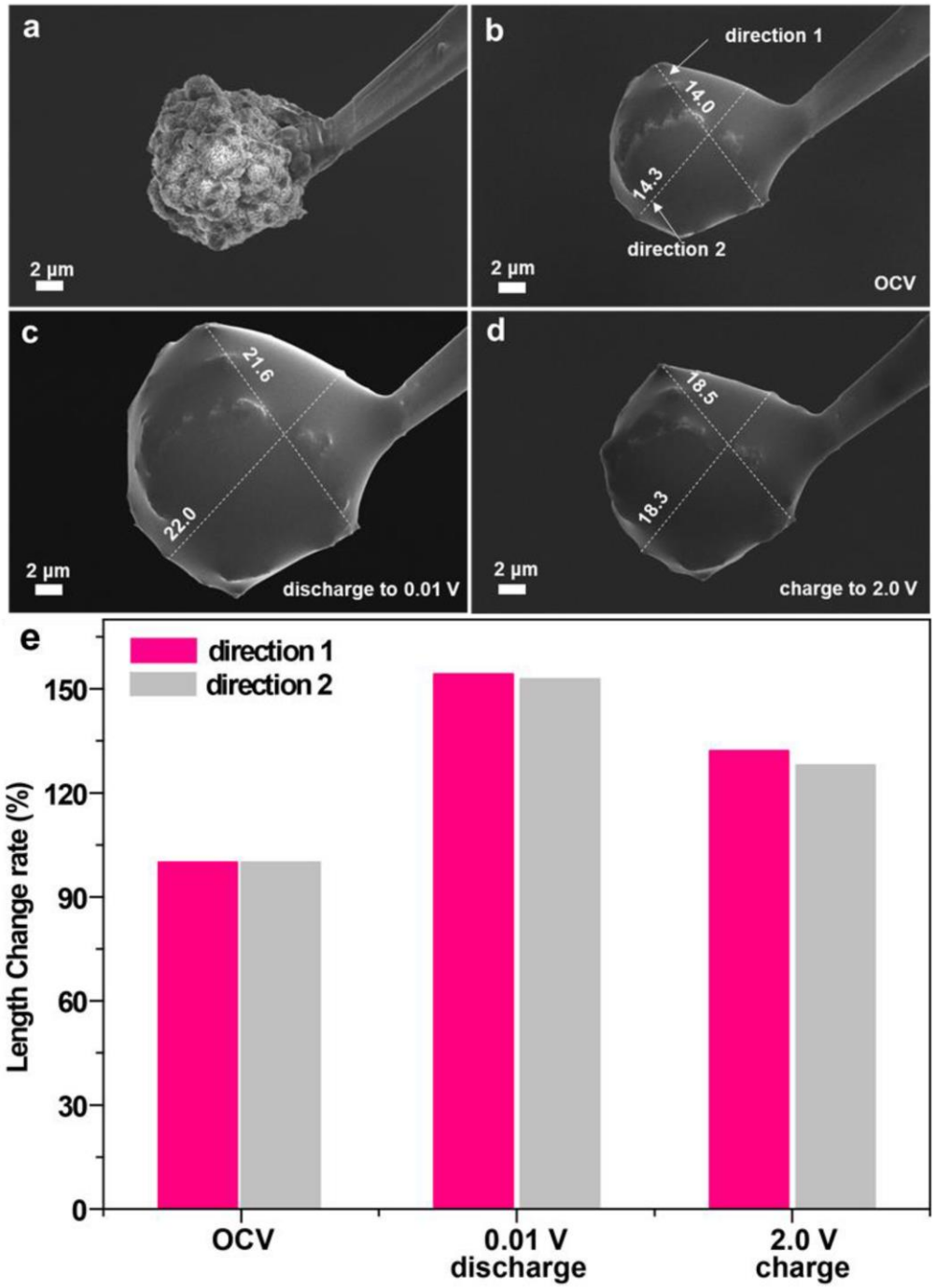

Figure S19. **(**a-d) *In situ* SEM images of the bare porous Ge particle under different potentials. (e) Length change of the bare porous particle in different stages. We defined the length of the two directions under open-circuit voltage of this particle as 100%.

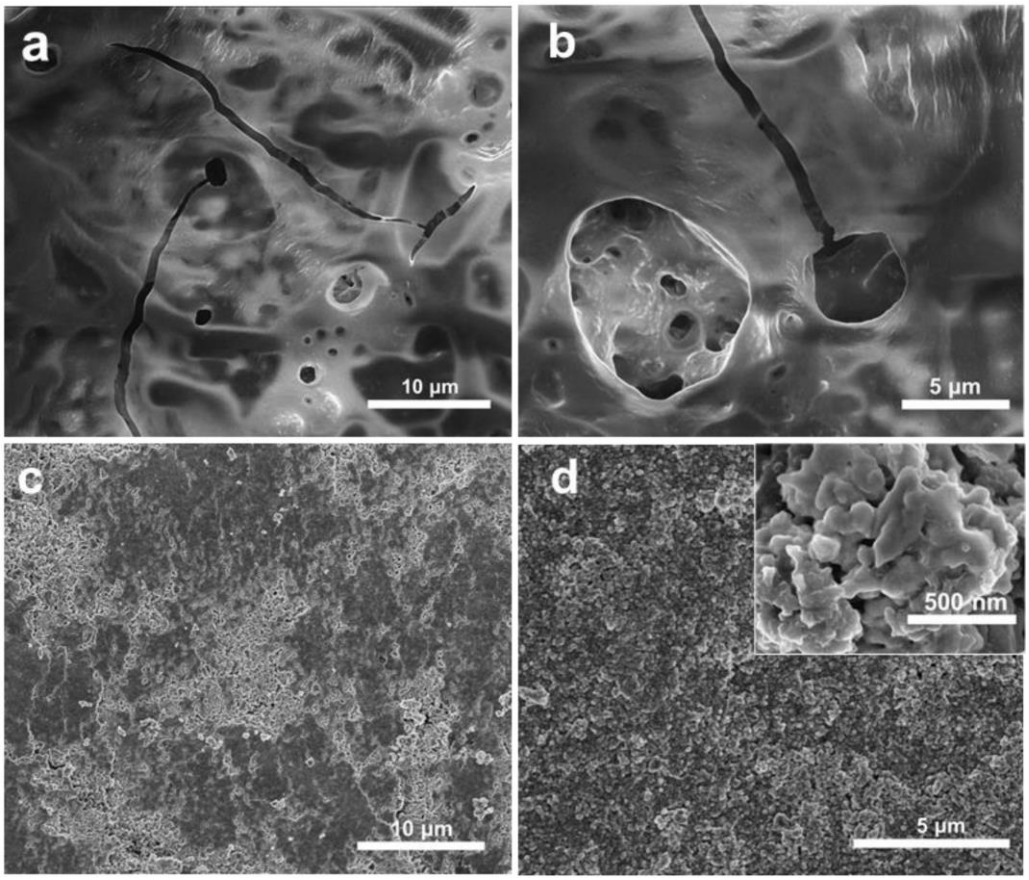

Figure S20. SEM images of (a, b) bare porous Ge and (c, d) Sb-coated-porous Ge electrodes after 20 cycles at current density of 1000 mA g^{-1}.

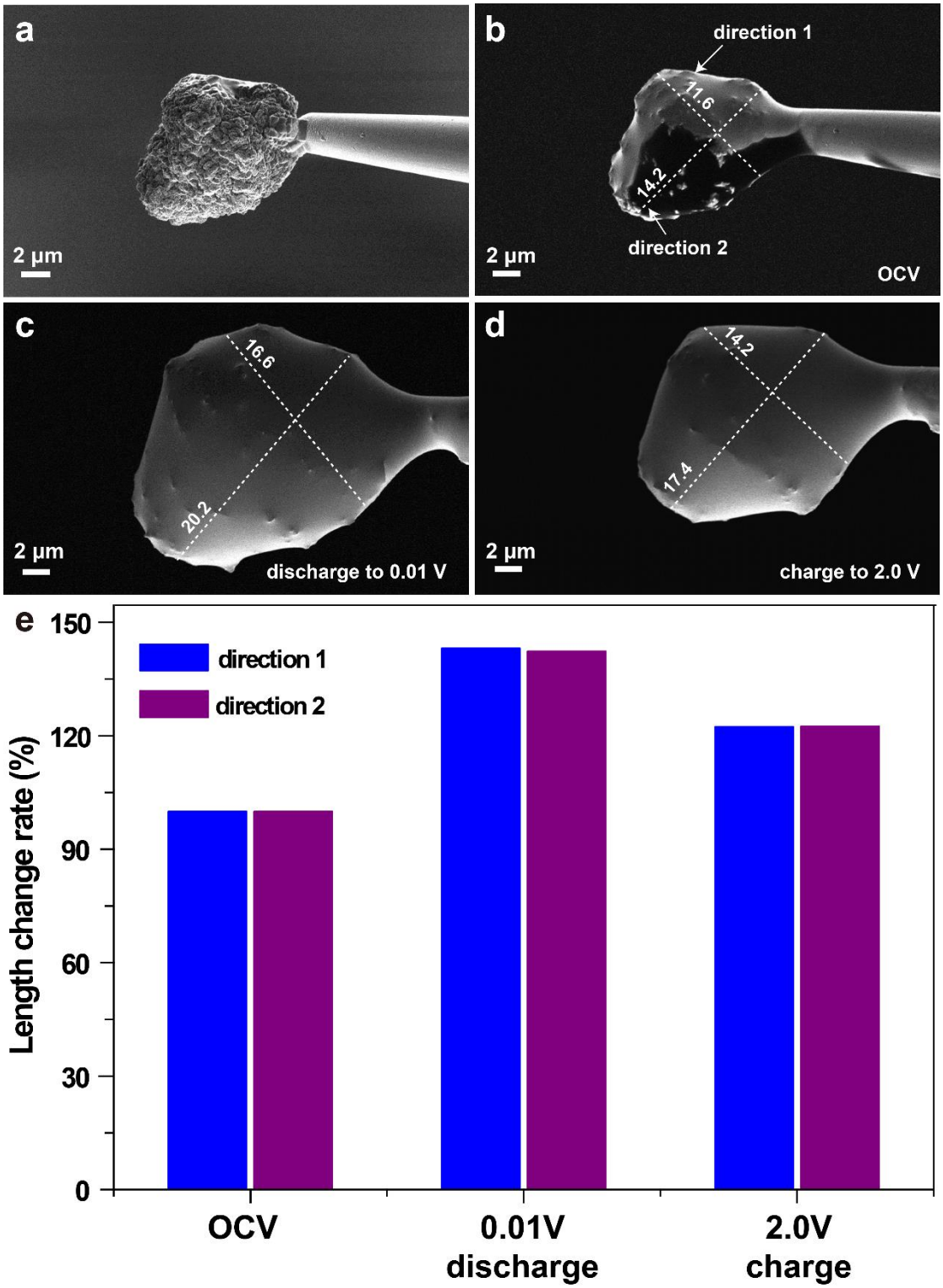

Figure S21. (a-d) *In situ* SEM images of the Sb-coated-porous Ge particle under different potentials. (e) Length change of the Sb-coated-Ge porous particle in different stages. We defined the length of the two directions under open-circuit voltage of this particle as 100%.

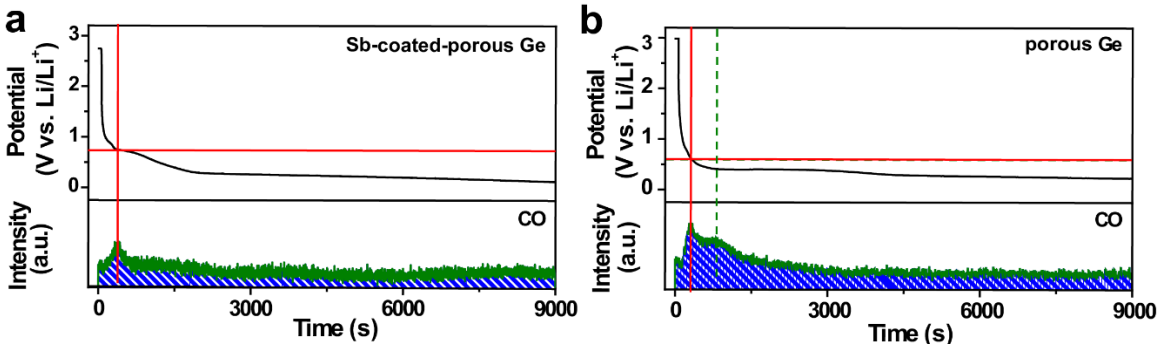

Figure S22. Plots of CO (m/z = 28) evolution for the initial discharge of the (a) Sb-coated-porous Ge and (b) porous Ge electrodes.

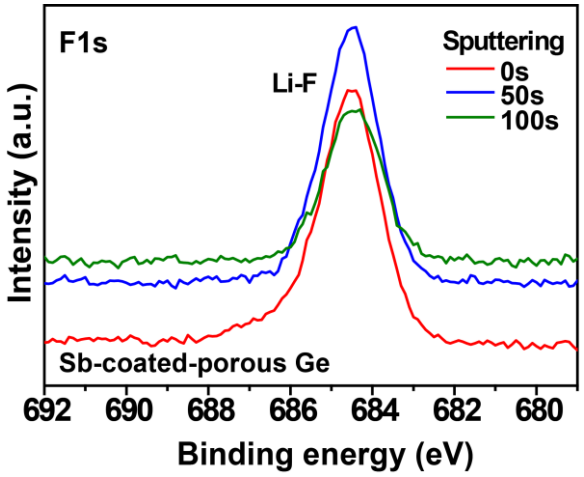

Figure S23. XPS analysis of fluorine without sputtering and with sputtering time of 50 and 100s for the Sb-coated-porous Ge electrode.

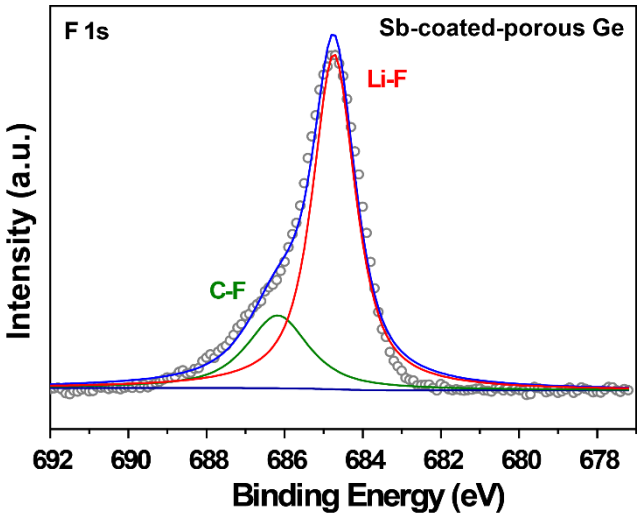

Figure S24. XPS analysis of F 1s at the initial discharge to 0.5 V for Sb-coated-porous Ge electrode.

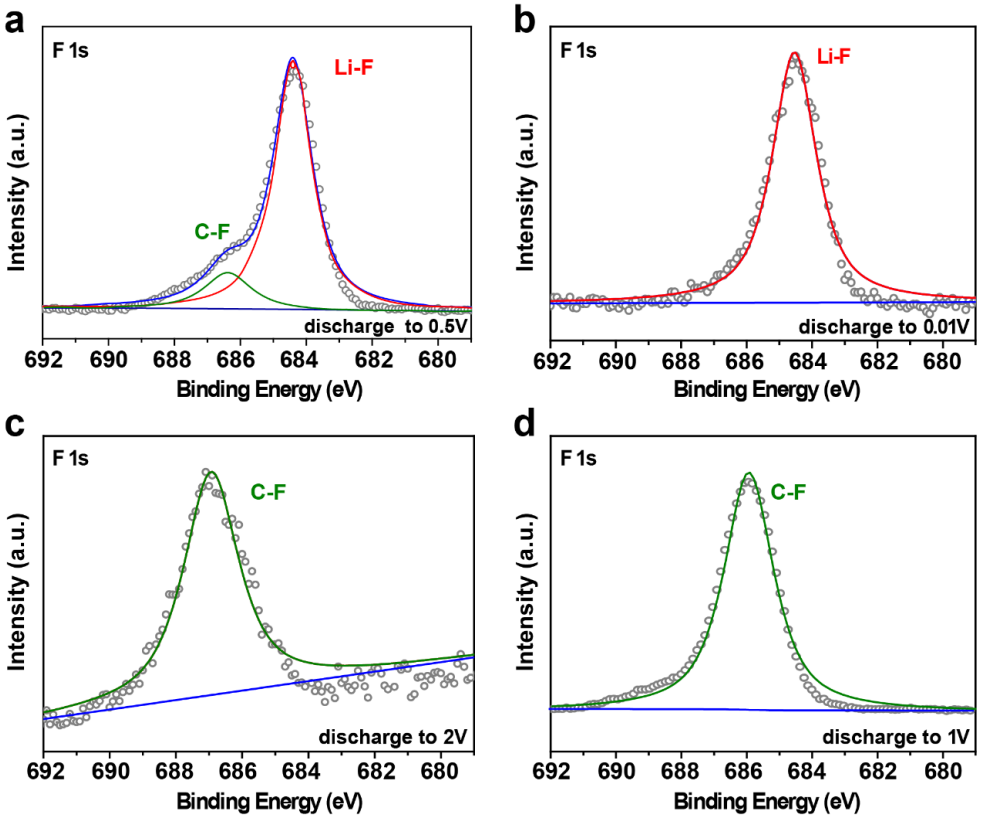

Figure S25. XPS analysis of F 1s at different discharge stages: (a) 0.5 V and (b) 0.01 V for Sb electrodes; (c) 2.0 V and (d) 1.0 V for porous Ge electrodes.

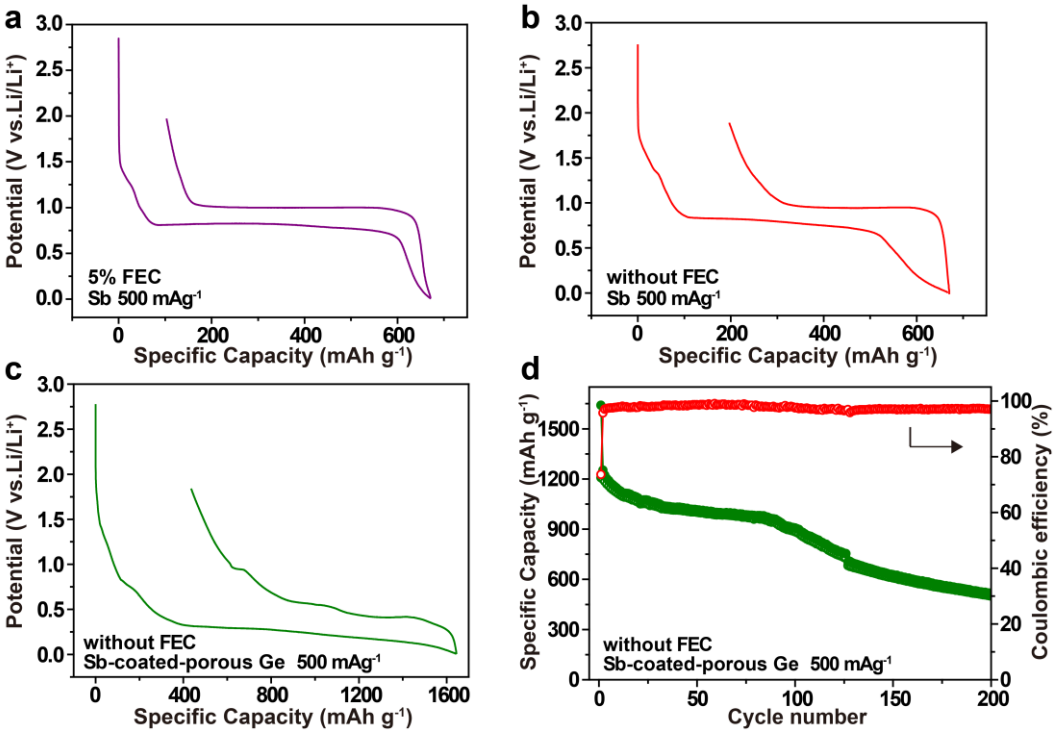

Figure S26. Initial potential profiles of Sb electrodes in electrolyte (a) with and (b) without FEC. (c, d) Initial potential profile and cycling performances of Sb-coated-porous Ge electrode in electrolyte without FEC.

Table S1 Binding energy (eV) of configurations of EC and FEC adsorbed parallel/vertical on the species' surface planes.

Adsorbed type	Species	Sb (111)-Li	Li_3Sb (111)	Ge (111)-Li	Li_3Ge (111)
Parallel	EC	-0.837	-0.645	-0.842	-0.549
	FEC	-0.753	-1.060	-0.776	-0.486
Vertical	EC	-0.762	-0.623	-0.684	-0.456
	FEC	-0.686	-0.581	-0.625	-0.417

Table S2. ICOHP of Li-O and Li-F bonds between EC/FEC molecules and Li_3Ge (111)/Li_3Sb (111) surfaces.

	Li_3Sb(111)-EC	Li_3Sb(111)-FEC		Li_3Ge(111)-EC	Li_3Ge(111)-FEC	
	Li-O	Li-O	Li-F	Li-O	Li-O	Li-F
ICOHP	-1.55	-1.50	-1.56	-1.57	-1.43	-1.39

Table S3 On-line electrochemical mass spectrometry analysis of the CO_2 gas product of two materials in the initial discharge.

Electrodes	Peak potential (V vs Li/Li^+)	Area (nmol g^{-1})
Porous Ge	0.60	323026
Sb-coated-porous Ge	0.75	193702

References

[1] V. L. Deringer, A. L. Tchougreeff, R. Dronskowski, *J. Phys. Chem. A* **2011**, *115*, 5461.

[2] R. Dronskowski, P. E. Blöchl, *J. Phys. Chem.* **1993**, *97*, 8617.